FLORE
Repository istituzionale dell'Università degli Studi di Firenze

Is the Actuator line method able to reproduce the interaction between closely-spaced Darrieus rotors? a critical assessment on

Questa è la Versione finale referata (Post print/Accepted manuscript) della seguente pubblicazione:

Original Citation:

Is the Actuator line method able to reproduce the interaction between closely-spaced Darrieus rotors? a critical assessment on wind and hydrokinetic turbines / Mohamed O.S., Melani P.F., Papi F., Balduzzi F., Bianchini A.. - In: ENERGY CONVERSION AND MANAGEMENT. - ISSN 0196-8904. - ELETTRONICO. - 293:(2023), pp. 117473.0-117473.0. [10.1016/j.enconman.2023.117473]

Availability:

The webpage https://hdl.handle.net/2158/1347996 of the repository was last updated on 2025-02-11T15:05:16Z

Published version:

DOI: 10.1016/j.enconman.2023.117473

Terms of use:

Open Access

La pubblicazione è resa disponibile sotto le norme e i termini della licenza di deposito, secondo quanto stabilito dalla Policy per l'accesso aperto dell'Università degli Studi di Firenze (https://www.sba.unifi.it/upload/policy-oa-2016-1.pdf)

Publisher copyright claim:

La data sopra indicata si riferisce all'ultimo aggiornamento della scheda del Repository FloRe - The above-mentioned date refers to the last update of the record in the Institutional Repository FloRe

(Article begins on next page)

14 July 2026

Is the Actuator Line Method able to reproduce the interaction between closely-spaced Darrieus rotors? A critical assessment on wind and hydrokinetic turbines

Omar S. MOHAMED, Pier Francesco MELANI, Francesco PAPI, Francesco BALDUZZI, Alessandro BIANCHINI*

Department of Industrial Engineering, Università degli Studi di Firenze
Via di Santa Marta 3, 50139, Firenze, Italy
Phone +39 055 275 8773
Fax + 39 055 275 8755
* alessandro.bianchini@unifi.it

Abstract

The deployment of multiple closely-spaced Darrieus turbines has recently gained interest in the academic and industrial sectors due to their potential to increase power output and wake recovery. However, the computational cost of accurate three-dimensional, blade-resolved CFD analyses rapidly becomes unfeasible as long as multiple rotors are added, putting emphasis on the need for a more practical, yet accurate, simulation method. Based on recent assessments, the Actuator Line Method (ALM) has been shown to represent the most interesting solution for Darrieus turbines' simulations. However, since the blade-flow interaction is not solved, no evidence was available to date on whether ALM can capture all the physical phenomena related to turbine mutual interaction.

In this study, the reliability and limitations of the ALM in simulating closely-spaced Darrieus turbines were assessed using two pairs of turbines with varying geometrical and operational characteristics, focusing on turbine loads, local flow field, and wake development. The results demonstrate that the ALM is effective for simulating twin-rotor Darrieus turbines, particularly at medium and high tip-speed ratios, providing satisfactory predictions of instantaneous blade loads and capturing the increase in torque due to the mutual interaction between adjacent rotors. The ALM is also able to accurately reproduce the flow field across the twin rotors, as demonstrated through Proper Orthogonal Decomposition (POD) analysis of the wake flow field. With an average simulation time of 7 h/rev/core, compared to 508 h/rev/core for blade-resolved CFD, this study provides evidence that the ALM is a low-cost and reliable tool for simulating closely spaced Darrieus turbines, thus representing the most suitable tool to develop new VAWT applications like floating wind turbines or hydrokinetic installations.

Keywords: Actuator Line Model (ALM), VAWT, Darrieus, Hydrokinetic Turbines, Computational Fluid Dynamics (CFD), Proper Orthogonal Decomposition (POD)

Nomenclature

Latin symbols

A	Turbine area	[m^2]
C_L	Lift coefficient	[-]
C_p	Power coefficient	[-]
D	Turbine diameter	[m]
k	Turbulent kinetic energy	[m^{2}s^{-2}]
L	Turbulent length scale	[m]
P	Power	[kW]
R	Turbine radius	[m]
Re_c	Chord-based Reynolds number	[-]
U	Matrix of snapshots	[-]
u_n	Left eigenvector	[-]
V_∞	Freestream velocity	[m·s^{-1}]
V_m	Right eigenvector	[-]

Greek symbols

β	Kernel width	[m]
Δh	Mesh element size	[m]
θ	Azimuth angle	[deg]
ρ	Flow density	[kg·m^{-3}]
$\sum$	Matrix of eigenvalues	[-]
σ_m	Eigenvalue	[-]
ϕ_n	Matrix of left eigenvectors	[-]
ϕ_V	Matrix of right eigenvectors	[-]
χ_n^m	Entries to the matrix of snapshots (dimensionless velocity fluctuations)	[-]
Ω	Vorticity	[s^{-1}]
ω	Rotor rotational speed	[rad·s^{-1}]

Acronyms

AC	Aerodynamic Centre	
ALM	Actuator Line Method	
AoA	Angle of Attack	[deg]
BSC	Blade-Spoke Connection	[-]
CFD	Computational Fluid Dynamics	
CSS	Cubic Spline Smoothing	
HAWT	Horizontal Axis Wind Turbine	
LES	Large Eddy Simulation	
POD	Proper Orthogonal Decomposition	
RANS	Reynolds-Averaged Navier-Stokes	
SST	Shear Stress Transport	
SVD	Singular Value Decomposition	
TSR	Tip Speed Ratio	[-]
VAHT	Vertical Axis Hydrokinetic Turbine	
VAWT	Vertical Axis Wind Turbine	

1. Introduction

1.1 Background and motivation

While the industry is still reluctant to invest in technologies for wind and tidal/hydrokinetic power deviating from the well-established three-blade horizontal-axis rotor, an increasing amount of research is pointing out that the vertical-axis concept has very interesting features for innovative installations. On the one hand, Vertical-Axis Wind Turbines (VAWTs) are very promising for offshore floating applications, both at the level of the isolated rotor, thanks to a lower center of gravity and therefore improved system dynamics [1], and at the wind farm one, as VAWTs can boost the farm energy harvesting by entraining momentum from the upper layers of the atmosphere [2]. On the other hand, Vertical-Axis Hydrokinetic Turbines (VAHTs) already represent a low impact and cost-effective solution for the exploitation of the so-called "hidden hydropower", i.e., the one coming from channels and small rivers [3]. In spite of these advantages, further research is currently required to improve the energy conversion efficiency of these machines and fill their gap with respect to their horizontal-axis counterparts. In this perspective, one key topic that has been studied extensively in the last years are array effects in closely spaced Darrieus machines; in fact, it has been observed that a VAWT rotor has a higher efficiency in a row than when it is isolated. This effect was first shown Dabiri [4]. Following his experimental campaign, several studies were conducted, mainly using two-dimensional Reynolds-Averaged Navier-stokes (RANS) simulations, to investigate the physical mechanisms underlying such performance enhancement [5]–[7]. The favourable deviation in the absolute inflow direction and wake contraction happening in the gap between the rotors were identified as responsible for power augmentation. Other studies focused on optimising the layout of the turbines in terms of spacing and relative angle between the rotors [8]–[10]. They concluded that the maximum power output could be achieved via the *in-line* arrangement, i.e., zero oblique angle between the rotors, and spacing between 1.5 and 1.8D. The few three-dimensional studies available to date, for example the one of Nazari et al. [11], indicated two-dimensional studies as optimistic in determining torque production and wake dissipation rate. This kind of simulations, nonetheless, is at the current state-of-the-art not feasible at a research and industrial level, due to prohibitive computational power requirements.

Therefore, the attention of the scientific community has been directed towards the development of low- or medium-order approaches, able to capture the main effect on performance and wake recovery of blade-resolved CFD, but at a notably lower computational cost. Low-order tools were proposed by Araya et al. [12], who developed an analytical model based on the Rankine body formulation, and Nishino et al. [13], who proposed a theoretical model to estimate the performance of tidal Darrieus turbine arrays within a finite-width channel. Although considered beneficial for the rough estimation of the energy output of a Darrieus turbine cluster, these models cannot capture the complex three-dimensional flow structures that occur either in the wake or in the mutual interaction region between the rotors. Tavernier et al. [14] employed a two-dimensional vortex model to study a pair of Darrieus wind turbines, while Gauvin-Tremblay and Dumas [15] developed the Effective Performance Turbine Model to investigate the local blockage effect in an array of VAHTs.

To have an insight on these aspects, CFD must therefore be reintroduced. This led to the development of the so-called "hybrid" methods that combine CFD to solve the flow field and a lumped-parameter aerodynamic model, usually based on input polar data, to compute the rotor forces, which are inserted in the computational grid as volume forces [16].

Among the hybrid simulation tools available, the Actuator Line Method (ALM) stands out for its accuracy and computational efficiency. Several studies [17]–[19], including contributions from the authors [20]–[22], have demonstrated the capability of this approach to simulate isolated Darrieus rotors. However, there are only a few studies in the literature that employ the ALM for multiple rotors. For example, Hezaveh et al. [23] used the ALM in conjunction with a Large Eddy Simulation (LES) model to evaluate the feasibility and performance of a VAWTs wind farm. While Raj used the ALM to investigate the spacings between two closely spaced rotors [24]. In a recent work by Zhang et al. [25], the ALM was coupled with RANS simulations to investigate the synergy effect of two and three VAWTs. It is worth noting that these latter studies were primarily focused on optimizing the cluster synergy effect or studying the wake on a farm scale, without critically investigating the ability of the ALM to capture the flow interactions that occur between closely deployed Darrieus rotors.

It is important to mention that the authors have extensively developed the ALM formulation utilized in this work by incorporating additional models tailored for VAWT rotors. This includes evaluating dynamic stall model settings [26], incorporating ad hoc models to account for blade-spoke connections and pitching moment [20], and verifying the use of the *LineAverage* method to sample the Angle of Attack (AoA) in VAWTs [27], [28]. Furthermore, a dedicated sensitivity analysis of this ALM formulation has been conducted recently to investigate the effects of kernel shape and size, as well as spatial sensitivity analysis to loads [22].

1.2 Novelty and contribution of the study

Moving from this background, the present study aims at understanding if a hybrid simulation model like the ALM, which cannot intrinsically capture higher-order fluid-dynamic phenomena like blade-vortices interaction, is anyhow able to cope with the complex array effects occurring when multiple rotors are deployed in close proximity, i.e., the suppression of the streamtube expansion effect in the gap between the rotors, together with the associated performance augmentation. These effects were extensively analysed using two-dimensional blade-resolved CFD in a recent study by the authors [29]. Proving that a computationally efficient method like ALM is suitable to this end is of particular industrial relevance, as it can become a new industry standard to promote the emerging technology of hydrokinetic turbines deployed in arrays. In particular, this represents the basic theoretical step needed to build upon when moving to three-dimensional simulations of real machines. To date, indeed, no prove that ALM could capture twin VAWT interactions was available.

The ALM tool developed over the years specifically for the simulation of vertical-axis turbines [20] [22] has been employed. The latter features a novel *LineAverage* (*LineAvg*) method for accurate AoA sampling, as well as advanced aerodynamic sub-models to account for phenomena typically associated with Darrieus turbines, such as dynamic stall, pitching moment deriving from the selected blade-spoke connection, and flow curvature. ALM simulations were performed for both a wind and an hydrokinetic rotor, and validated against the blade-resolved CFD data from Zanforlin et al. [5] and from a recent work of the authors [29], respectively. The comparison of the two datasets was carried out in terms of:

a. *turbine performance*, in terms of overall performance and torque profiles over a revolution;
b. *flow kinematics,* with particular reference to the local AoA and velocity magnitude, which were sampled from both ALM and blade-resolved simulations via the *LineAverage* sampling approach [30], recently validated by the authors for the use on vertical-axis turbines [16];
c. *wake development.* One of the elements of novelty of the present study is the use of Proper Orthogonal Decomposition (POD) to analyze the capability of the ALM to reproduce the wake of closely-spaced Darrieus turbines. Such information is of capital relevance for many potential applications, including high-power-density wind farms based on VAWTs [31] or arrays of hydrokinetic turbines to be installed in channels or rivers [32].

1.3 Structure of the study

The structure of this study is as follows. Section 2 provides details on the geometrical and operational characteristics of the selected test cases. In Section 3, the characteristics of the different numerical methodologies used herein are presented, including a brief description of the ALM base formulation, CFD set-up, and the adopted POD model. The results are presented in Section 4, where comparisons between the blade-resolved RANS results and the ALM are presented in terms of power coefficient, local flow kinematics, and wake flow field. Section 5 discusses the results, highlighting their relevance to go beyond the current state-of-the-art. Finally, Section 6 provides the conclusions and outlines potential future work.

2. Test cases

In the present study, two different configurations of twin Darrieus rotors were used as case studies. More specifically, analyses refer to:

- *3B-VAWT - WindSpire*: a 3-blade Darrieus VAWT that has been extensively tested for different configurations of closely-spaced rotors. Pioneering field measurements were reported by Dabiri et al. [4], in addition to the two-dimensional blade-resolved RANS results reported by Zanforlin et al. [5], and the results of Hezaveh et al. [23], which have been produced using a different formulation of the ALM. In the present study, only the two dimensional blade-resolved CFD results of [5] have been used as benchmarking data to validate the current ALM formulation;
- *2B-VAHT – HE-PowerGreen*: an industrial prototype of 2-blade Darrieus VAHT early presented in [32], for which multiple design configurations have been investigated in previous works [3], [29]. It has been also studied in [21], where an investigation on a possible active pitch control strategy has been conducted using ALM. In this study, a set of dedicated twin-rotors, blade-resolved RANS simulations have been carried out to be used for the ALM validation.

The corresponding geometrical and operational characteristics for the two rotors are reported in Table 1. The selection of these test cases was justified by the quantity and quality of benchmark data available, as well as the corresponding variety of rotor solidities, working fluid (air vs. water), blade Reynolds number ranges. In this perspective, the validation is thought to be as general as possible. It is worth noticing that, while having different solidity, both test cases fall in the medium solidity range, which is particularly indicated for hybrid simulation models, as their accuracy in fact strongly decreases going toward high-solidity configurations [33].

The operating conditions of interest were selected so that the ALM tool could be assessed in different modes of operation. For the *3B-VAWT* rotor, two operating points were picked, the optimum TSR=2.7, where the dynamic stall is relevant, and TSR=3.2, where blockage effects are dominant. On the other hand, for the *2B-VAHT* rotor, TSRs of 2.5 and 3 were selected. TSR = 3 is the optimum operating point for twin rotors as concluded in [29], while at TSR = 2.5, a significant impact of dynamic stall is apparent, and has been successfully modelled for a stand-alone configuration in [20].

Table 1: Operational and geometrical characteristics of the turbine pairs used in the present work.

Variable	3B-VAWT	2B-VAHT
Airfoil shape	DU06W200	DU06W200 (reversed)
Number of blades [#]	3	2
Diameter [m]	1.2	2

Chord [m]	0.128	0.25
Solidity (nc/D) [-]	0.32	0.25
Tip Speed Ratio (TSR) [-]	2.7 – 3.2	2.5 - 3
Centre-to-centre spacing [-]	1.5D	2.5D
Freestream velocity [m/s]	8	2

3. Methodology

3.1 Actuator Line Method

The Actuator Line Method (ALM) [16] is a computational tool that is being extensively used for simulating wind turbines. The corresponding workflow is the following. First, the position of the actuator line corresponding to the turbine blade is located on the computational grid. Then, the blade Reynolds number and angle of attack are sampled from the local flow field and are combined with the available polar data and sub-models to compute the corresponding aerodynamic forces. The latter are eventually projected into the computational domain as momentum source terms in the Reynolds-Averaged Navier-Stokes (RANS) solver. In the present work, the ALM tool developed over the years by the authors and tailored to the simulation of vertical-axis turbines [20] has been adopted and set-up as following:

- *Sampling of the local flow field:* the *LineAverage* method is used to estimate the blade angle of attack (AoA) from the local flow field. Originally proposed for horizontal-axis wind turbines by Jost et al. [30] and validated by the authors for the application to vertical-axis turbines [27], [28] , this method calculates the undisturbed velocity as an integral average of the velocity field along a closed line around the airfoil. In the present study in particular, a circular line with a radius of r = 1c, N = 80 equally spaced points and centered on the airfoil quarter-chord is used. Moreover, to reduce the background noise, a low-pass filtering is applied to the sampled data using a Cubic Spline Smoothing (CSS) algorithm [34], according to the procedure outlined in [26];
- *Pitching moment and BSC corrections:* to account for two phenomena specific to vertical-axis turbines, ad hoc corrections are applied to the predicted torque. First, since the pitching moment of the airfoil acts in the blade rotational plane, an additional contribution is included in the shaft torque computation [35]. Second, in the cases where the Blade-Spoke Connection (BSC) point of the blade support strut does not coincide with the blade's AC, the AoA and load distribution must be modified accordingly [18], [19]. It is worth noting that, for the selected test case, the blade is mounted at the quarter-chord and thus the latter correction has no effect (see Table 2);
- *Polar data*: the accuracy of the ALM code in predicting the performance of a rotor depends on the quality of the polar data used. This is particularly important for small Darrieus rotors, such as the ones considered in the present study, where the Reynolds numbers are relatively low, and the impact of laminar separation bubbles on the aerodynamic performance of the airfoil is more significant. In addition, one should remember that, as any other method that makes use of tabulated data to model blade aerodynamics, the use of data referring to the virtually transformed airfoil deriving from virtual camber correction are mandatory [36]. In the present case, pre-stall aerodynamic coefficients for both rotors were determined using the viscid panel method software XFoil [37], which proved to be robust when benchmarked against more complex methods. Additionally, both sets of data were extended over the deep stall region, up to an angle of attack of ±180°, using the Viterna-Corrigan model [38], as recommended by Bianchini et al. [39] for Darrieus turbines applications;
- *Berg dynamic stall model*: the present code incorporates the dynamic stall model proposed by Berg [40] to accurately capture the impact of unsteady flow on the blade loads, as explained in [26]. This model introduces a delay in the measured angle of attack proportional to the flow reduced frequency to embed dynamic effects in the solution. The lift and drag coefficients are obtained as a linear interpolation between the static and dynamic coefficients, weighted over the constant A_M. The A_M values were fine-tuned to be 6 and 20 for *3B-VAWT* and *2B-VAHT* twin rotors, respectively, following the procedure described in [26]. To determine the stall angle, which is a crucial step in determining the slope of the lift curve in the pre-stall region, two methods were evaluated in the previous work discussed in [26]. The first method, *MaxLift*, selects the static stall angle as the point

of maximum lift in the pre-stall region, following the same approach used to extend the polar data in the post-stall region. The second method, *LinReg*, selects the static stall angle as the angle giving the line that best approximates the lift curve in the pre-stall region. The former method is straightforward to implement when the operating Reynolds number is high enough to keep the lift behavior nearly linear during the pre-stall region. In contrast to the *MaxLift* which can be beneficial when the operating chord-based Reynolds number is low, and the pre-stall lift behavior is nonlinear due to the presence of a viscous separation bubble. Considering the range of the operating Re_c for the current case studies, for *3B-VAWT* rotors, *MaxLift* was used, while *LinReg* was implemented for the *2B-VAHT* twin rotors.

Additional information about the code formulation can be found in [20].

Regarding the *Frozen ALM* approach, this was originally introduced by [41], and has been recently used by the authors to study the impact of the Regularization Kernel function for a single Darrieus rotor [22]. This approach, while not specifically thought for design (since aerodynamic coefficients data coming from blade-resolved CFD are needed) is of particular use whenever one needs to differentiate the errors stemming from the aerodynamic coefficients or dynamic stall model and those resulting from other factors such as the projection function, angle of attack (AoA) sampling, spatial or temporal discretization. In this study, the Frozen ALM is employed in the wake analysis section to effectively identify the sources of discrepancies between the ALM wake and that of the blade-resolved CFD.

3.2 CFD setup

Two-dimensional simulations were performed using the unsteady Reynolds-Averaged Navier-Stokes (URANS) method, employing the commercial software ANSYS® FLUENT® in its 2020 R2 release. The selected turbulence closure model was the *k-ω* Shear Stress Transport (SST) model, renowned for its accuracy and stability in unsteady flow conditions. These conditions frequently arise in VAWT blades, where significant flow separations and pressure gradients occur [42]. It is worth noting that the y^+ value for all blade-resolved CFD cases remained below 1, satisfying the prerequisites of the SST model.

Furthermore, other simulation details, including the domain, grid, and time stepping sizes, were consistent for both the blade-resolved CFD and the ALM. The pressure-based solution was employed using a coupled algorithm, and a second-order upwind scheme was utilized for the spatial discretization of all transport equations. The time differencing employed a bounded second-order implicit scheme. Additionally, the residuals for all variables were set to 10^{-5}, and 30 inner iterations were performed per time step. These simulation settings were chosen based on comprehensive sensitivity analyses conducted by some of the authors, as referenced in [43], [44].

For a detailed description of the blade-resolved CFD setup, please refer to the authors' latest publication in [29]. The CFD domain, boundary conditions, and grid details for the ALM are reported and discussed in the subsequent sub-sections.

3.2.1 Domain and boundary conditions

The computational domain was an open field, with its dimensions parametrized with respect to the turbine diameter D as shown in Figure 1. The partitioning and sizes of the wake zones were established following the approach outlined in [45]. This methodology aimed to minimize flow disturbances caused by the turbine, thereby justifying the use of standard far-field boundary conditions commonly employed in external flow simulations.

To ensure the numerical independence of the solution from the domain size, a domain sensitivity analysis was performed. Different test cases with varying domain sizes were evaluated for the 2B-VAHT, as reported in Table 2, which also includes the domain size of the blade-resolved CFD evaluated on an ALM case. Figure 2 presents the results of the domain sensitivity assessment in terms of the instantaneous torque coefficient, C_T, and coefficient of determination, R^2. Some of the authors have introduced R^2 as a criterion for evaluating the spatial or temporal numerical independence, as described in [44]. This criterion considers both the instantaneous and average values of the errors. In this case, R^2 was calculated as follows:

$$R^2 = 1 - \frac{\sum_{\theta=0°}^{360°}\left[C_T(\theta) - C_{T,final}(\theta)\right]^2}{\sum_{\theta=0°}^{360°}\left[C_T(\theta) - C_{T,avg.}\right]^2} \quad (1)$$

where $C_T(\theta)$ represents the instantaneous torque coefficient of a given case, $C_{T,final(\theta)}$ denotes the instantaneous torque coefficient of the largest domain case, D(BR-CFD) in the present analysis, and $C_{T,avg.}$ represents the average torque over a full revolution. From the results shown in Figure 2, no significant differences can be observed between D02, D03, and D(BR-CFD). Notably, the R^2 value for D02 is above 99.9%. Based on these findings, the domain dimensions of D02 were selected for the subsequent simulations.

Regarding the boundary conditions, uniform values were prescribed at the inlet for velocity (8 m/s for the 3B-VAWT and 2 m/s for the 2B-VAHT), turbulent kinetic energy (k), and length scale (L), tailored to match the testing conditions of the specific test case. The turbulent quantities were estimated based on the inlet turbulent intensity and length scale. For the 3B-VAWT, a turbulent intensity of 4% with a length scale of 1 m was set, while for the 2B-VAHT, a turbulent intensity of 0.25% with a length scale of 2.84 m was used. As for the outlet boundary, a uniform atmospheric pressure was specified, and a symmetry condition was enforced on the other boundaries.

Table 2: Test cases for the sensitivity analysis on domain dimensions

Case	D1	D2	D3	D(BR-CFD)
L1/D	10	15	20	20
L/D = (L1 + L2)/D	30	45	60	80
W/D	20	30	40	42
Aspect ratio (L/W)		1.5		1.9

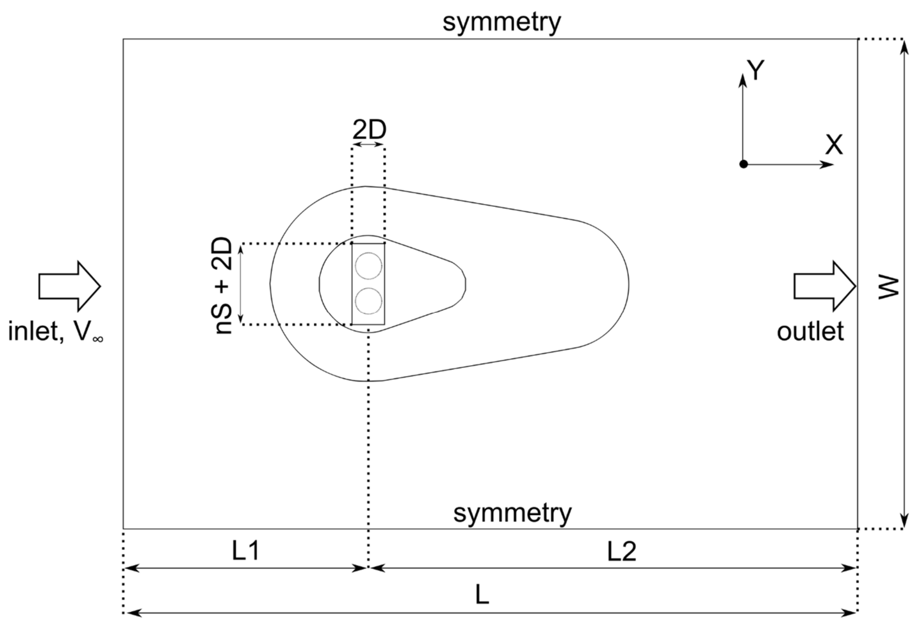

Figure 1 - Computational domain and boundary conditions.

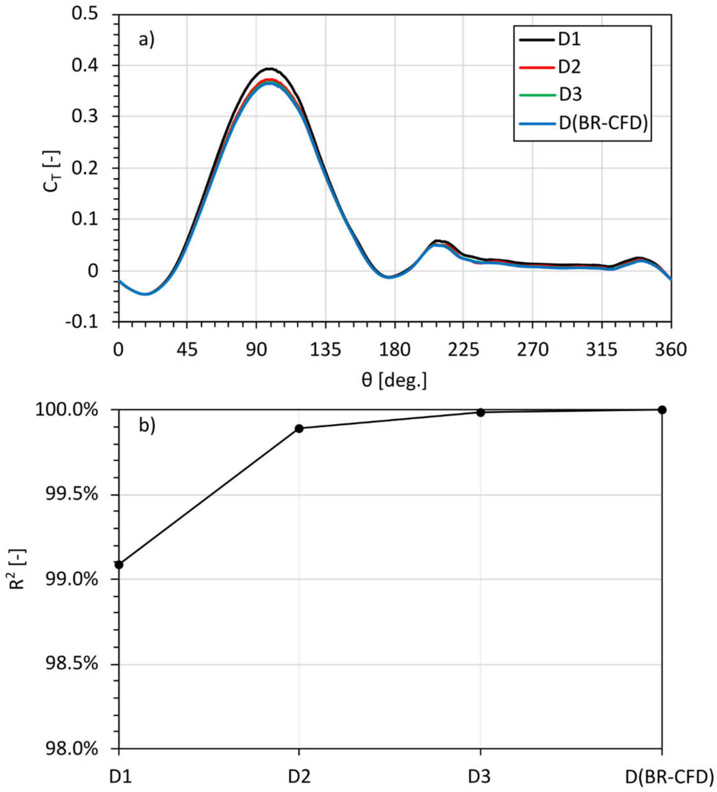

Figure 2 - Results of domain independence test for 2B-VAHT pair at TSR = 3: a) instantaneous torque coefficient and b) coefficient of determination

3.2.2 Computational grid

A hybrid meshing strategy was employed to discretize the CFD domain into three separate fluid zones based on the main features commonly found in a Darrieus turbine operating in an *open-field* environment. The first zone is the rotor ALM region, which encompasses the turbine rotor and is discretized with a structured mesh to fulfil the requirements of the ALM. The second zone is the wake region, which requires an unstructured quad-dominant mesh to capture the turbine blockage and wake development. This region is divided into a near-wake and a far-wake zone. The near wake region is extended 6D downstream, while the far wake region is 16D downstream.

In a previous study [22], a grid independence test was performed by the authors to determine the optimal mesh resolution in the ALM region based on turbine loads. The conclusion drawn from that study was that $\Delta h_{ALM} = \beta/1.5$ provides a favourable balance between accuracy and computational time, where β represents the kernel width ($\beta = 0.25c$). However, in the current analysis, two separate grid independence tests were conducted, focusing on both the ALM and wake regions.

The first grid sensitivity assessment aimed to ensure that load estimation remains independent of the grid size, and to validate the conclusions reached from the single rotor analysis for the twin rotor analysis as well. In this test, different cases with varying mesh sizes are presented in Table 3, where different element sizes were implemented in the ALM region. The meshing strategy in this assessment follows that of the single rotor analysis reported in previous studies. Specifically, the near wake region is always taken as double the size of the ALM region ($\Delta h_{NearWake} = 2\Delta h_{ALM}$), while the far wake region is double the size of the near wake region ($\Delta h_{FarWake} = 2\Delta h_{NearWake}$).

The second grid sensitivity analysis focused on the wake regions, where the element size in the ALM region remained constant while different grid sizes were applied to the near wake region, $\Delta h_{NearWake}$. The element size in the far wake region was consistently set at twice the size of the near wake region across all tested meshes. The specific details of the evaluated meshes can be found in Table 4.

Figure 3 presents the results of the mesh independence tests. On the top left side of the figure, the results of the first grid assessment are shown in terms of the instantaneous torque coefficient, it is important to note that here, all the cases reached an $R^2 > 99.9\%$. However, increasing the grid size in the ALM region above β/1.5 lead to volatility in the calculated load as highlighted at $75° < \theta < 120°$, as observed also before for the single rotor [22]. Therefore, the results of the first grid independence test led to the conclusion that $\Delta h_{ALM} = \beta/1.5$ is the optimal mesh size. Thus, G1.2 was selected for the subsequent grid independency test. On the right side of Fig. 2, the results of the wake grid sensitivity analysis are illustrated in terms of velocity profiles at X/D of 1 and 3. The solid and dashed lines represent the coefficient of determination, R^2, for the velocity profiles. In this test, R^2 was calculated as:

$$R^2 = 1 - \frac{\sum_{Y/D=-2.5}^{2.5}\left[V(Y/D) - V_{final}(Y/D)\right]^2}{\sum_{Y/D=-2.5}^{2.5}\left[V(Y/D) - V_{avg.}\right]^2} \qquad (2)$$

where *V(Y/D)* represents the local velocity value at a specific Y/D for the given mesh, $V_{final}(X/D)$ indicates the local velocity value of the finest mesh (G2.4 in this case), and V_{avg} denotes the average velocity along the given mesh. At X/D = 1, all grids exhibit identical velocity profiles. However, at X/D = 3, slight variations can be observed, with G2.3 displaying an R^2 value exceeding 99.9%. Based on these findings, G2.3 was chosen for subsequent simulations. Figure 4 illustrates the final selected mesh, including the representation of the mesh zones. Additionally, Table 5 presents a comparison between the blade-resolved CFD model and the ALM in terms of spatial and temporal discretization.

Table 3 - Tested grids for the ALM region mesh sensitivity analysis.

Case	Δh_{ALM}	No. of elements
G1.1	β	83,538
G1.2	β/1.5	180,639
G1.3	β/2	313,777

Table 4 - Tested grids for the wake zone mesh sensitivity analysis.

Case	$\Delta h_{NearWake}$	No. of elements
G2.1	$3\Delta h_{ALM}$	104,258
G2.2	$2.5\Delta h_{ALM}$	131,277
G2.3	$2\Delta h_{ALM}$	180,639
G2.4	$1.5\Delta h_{ALM}$	285,777

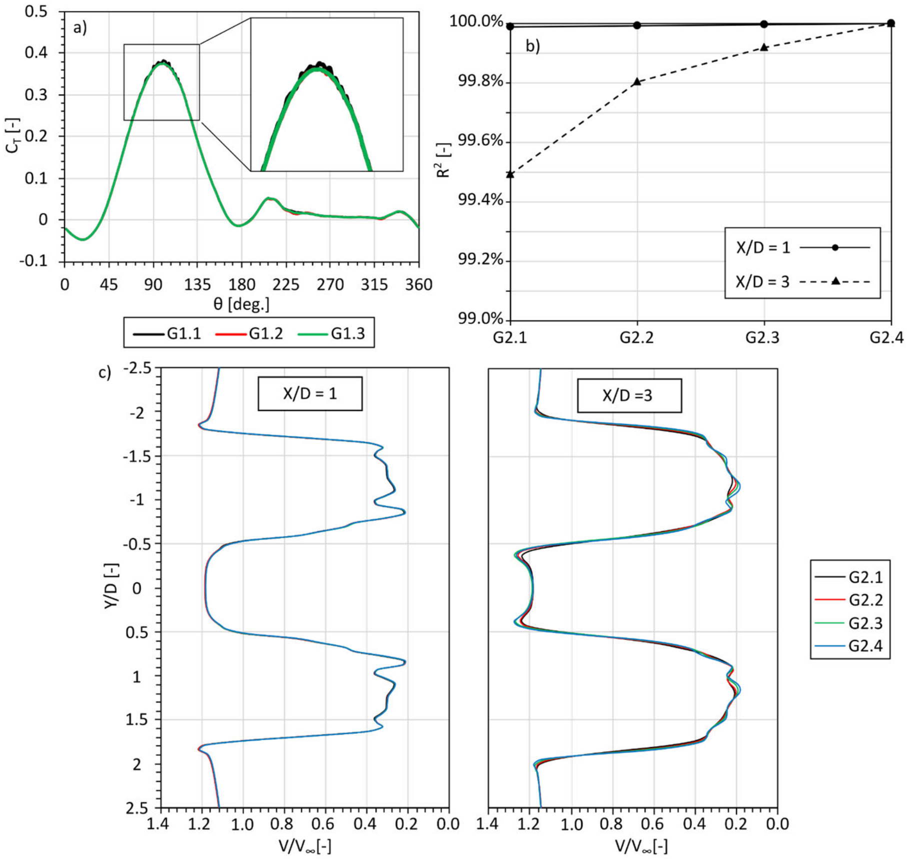

Figure 3 - Comparison between the different grid resolutions in terms of a) torque coefficient, b) coefficient of determination, and c) velocity profiles for the 2B-VAHT pair at TSR = 3 at X/D = 1 and 3.

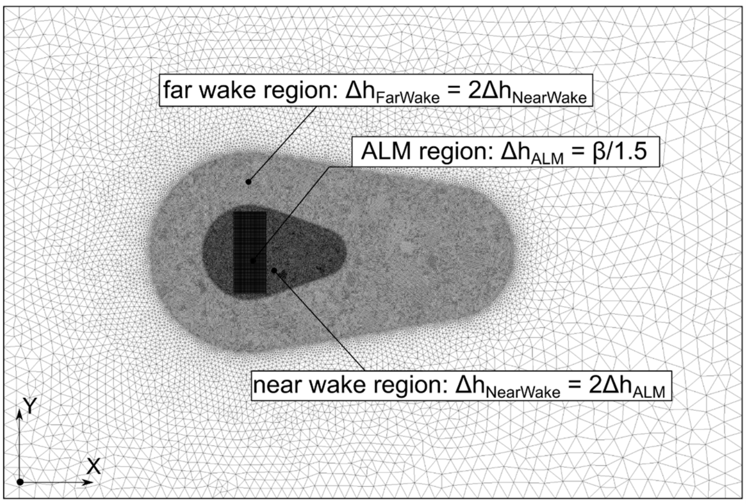

Figure 4 - Details of the computational grid.

Table 5 - A comparison of the numerical settings between the blade-resolved CFD and ALM simulations.

Numerical parameter	Blade-resolved CFD	ALM
Grid number of elements	1,016,848	180,639
Domain size	42D × 90D	30D × 45D
Angular step size (Δθ)	0.4°	1°

3.3 Proper Orthogonal Decomposition (POD)

POD is a powerful tool for analysing transient flow fields due to its ability to identify the main coherent spatial structures, or modes, contributing to the flow behaviour. Each mode represents a distinct spatial pattern, with a corresponding temporal coefficient that describes its time evolution. The modes are ordered based on their energy levels, with the first few modes typically capturing most of the flow dynamics [46]. POD has been recently employed to study the wake behind wind turbines. For example, Chen et al. [47] utilized RANS turbulence models to investigate the effect of gurney flaps on the performance of an H-shaped Darrieus VAWT. More recently, Sheidani et al. [48] used the POD to compare between RANS and LES simulations for a Darrieus hydrokinetic turbine.

In the present work, POD was applied to both simulations, in order to compare the wakes produced by the blade-resolved CFD and the ALM. More in detail, the flow field data at each spatial point on the two-dimensional domain was stored into a unit vector, χ_n^m , where n is the number of spatial points available, and m is the number of timesteps. Each value of χ_n^m is the fluctuating component of the velocity magnitude, obtained by removing the mean value from the instantaneous one. In this way, an $n \times m$ matrix U could be formed as:

$$U = \begin{bmatrix} \chi_1^1 & \cdots & \chi_1^m \\ \vdots & & \vdots \\ \chi_n^1 & \cdots & \chi_n^m \end{bmatrix} \tag{1}$$

This matrix is then decomposed via Singular Value Decomposition (SVD) into three other matrices, two of which contain the coherent structures in the spatial and temporal domains, in addition to the matrix of eigenvalues:

$$U = \phi_u \Sigma \phi_V^T = \begin{bmatrix} \vdots & & \vdots \\ u_1 & \dots & u_n \\ \vdots & & \vdots \end{bmatrix} \begin{bmatrix} \sigma_1 & 0 & 0 \\ 0 & \ddots & 0 \\ 0 & 0 & \sigma_m \end{bmatrix} \begin{bmatrix} \dots & V_1^T & \cdots \\ \dots & V_2^T & \dots \\ \dots & V_m^T & \dots \end{bmatrix} \tag{2}$$

where ϕ_u is the left eigenvectors matrix that contains the spatial coherent structures in the *n* points, while ϕ_V^T is the right eigenvectors matrix, physically representing the evolution of each mode in the *m* points. Σ, on the other hand, is a diagonal matrix of singular values, σ, organized in descending order, allowing the ordering of spatial modes in ϕ_U based on the corresponding energy level. As most of its energy is usually contained in the first few modes. The singular values are the square roots of the eigenvalues of the covariance matrix of the original data matrix, *U*. The percentage of energy corresponding to each mode is then computed as the square of the corresponding singular value divided by the sum of the squares of all singular values. From the statistical point of view, this quantity is equivalent to the total variance of the data explained by each mode. From the physical one, it corresponds to the total kinetic energy generated due to the velocity fluctuations in each mode.

The use of POD allowed to identify the core differences between the wakes predicted by ALM and blade-resolved CFD, thus providing a deeper understanding of how each formulation influences the wake development. In this study, the POD analysis was conducted within a selected area spanning 6D in the crosswind direction and 5D in the streamwise direction, located 1D downwind from the centre of the rotors as indicated in Figure 5. Instantaneous velocity magnitude data were stored for the three cycles after the 50th revolution to ensure that the flow field had reached a steady-state periodic condition past the turbines. It should be noted that the POD analysis was only carried out on the *2B-VAHT* rotor due to the availability of detailed flow fields from blade-resolved simulations.

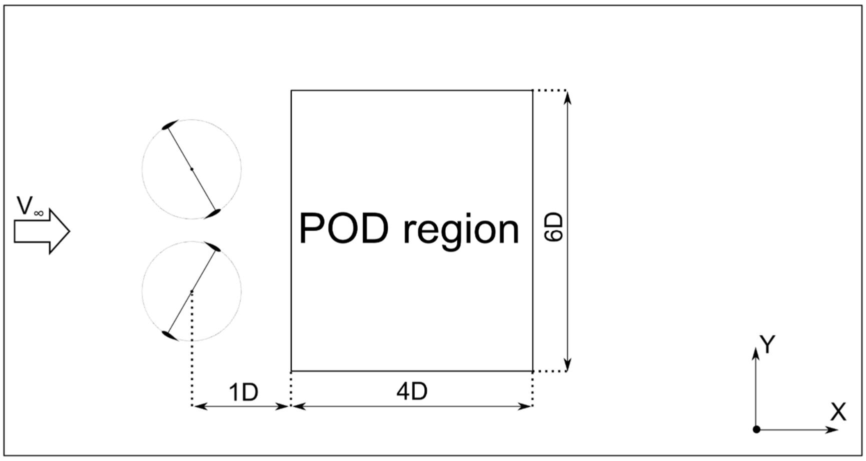

Figure 5 - POD analysis region.

4. Results

The results are reported in this section for both the *3B-VAWT* (section 4.1) and the *2B-VAHT* (section 4.2) twin rotors. In each section, the load results are firstly compared to those of blade-resolved CFD in terms of power and torque coefficients (C_P and C_T, respectively). The C_P is defined as the ratio of power, P, extracted by the turbine to the power available in the wind, while the C_T is the dimensionless torque on the blades:

$$C_p = \frac{P}{0.5\rho A V_\infty{}^3} \tag{4}$$

$$C_T = \frac{T}{0.5\rho A R V_\infty{}^2} = \frac{C_P}{TSR} \tag{5}$$

Secondly, the results of the local flow kinematics are reported and compared to that of the blade-resolved CFD. For the *3B-VAWT*, the local velocity profile was sampled at a certain azimuth position and compared to the data published by Ref. [5]. While for the *2B-VAHT*, this assessment was conducted by comparing the instantaneous angle of attack results. Finally, the wake flow field was investigated for only the *2B-VAHT* due to the data availability. This was carried out by initially reporting the velocity profiles at different downwind distances, followed by a POD analysis where the coherent spatial modes resulting from both the ALM and blade-resolved CFD simulations are compared.

4.1 Three-blade VAWT: *3B-VAWT*

This section presents the simulation results of the *c*, a three-bladed VAWT with medium solidity, to evaluate the ALM capabilities in simulating the performance of twin-rotor VAWTs. The results of this rotor pair include both inward and outward modes of rotation, with a distance of 1.5D between the two rotors. The operating range of this turbine is limited to relatively low chord-based Reynolds numbers, ranging from 130k to 290k within the assessed TSRs of 2.7 and 3.2.

4.1.1 Blade loading

For the *inward* configuration, the blade loading of the *3B-VAWT* turbine at TSRs of 2.7 and 3.2 were analysed using the ALM. Figure 6 shows the profile of blade torque coefficient (C_T) along one revolution, averaged over the two rotors. The results obtained from ALM were compared with the corresponding blade-resolved RANS simulations of Zanforlin et al. [5]. Additionally, the single rotor results, including those obtained from the single rotor ALM, were reported to provide a basis for comparison.

At TSR = 2.7, the results showed that the ALM was able to reconstruct the trend of the torque coefficient profile in the *upwind* region ($0° \leq \theta \leq 180°$), capturing the azimuthal position of the peak torque with a slight overestimation in its magnitude compared to the reference data. In the *downwind* section ($180° \leq \theta \leq 360°$), nonetheless, the ALM achieved a fair prediction of the torque coefficient trend, although overestimating energy extraction along the whole blade path between $\theta = 180°$ and $\theta = 360°$. At TSR = 3.2, in the *upwind* half, the trend of the torque coefficient profile matched that of the blade-resolved CFD, although with a slight lead of approximately 5°. Unlike at TSR=2.7, the ALM provided a satisfactory estimation of the *downwind* torque, although still slightly overestimated with respect to the reference data.

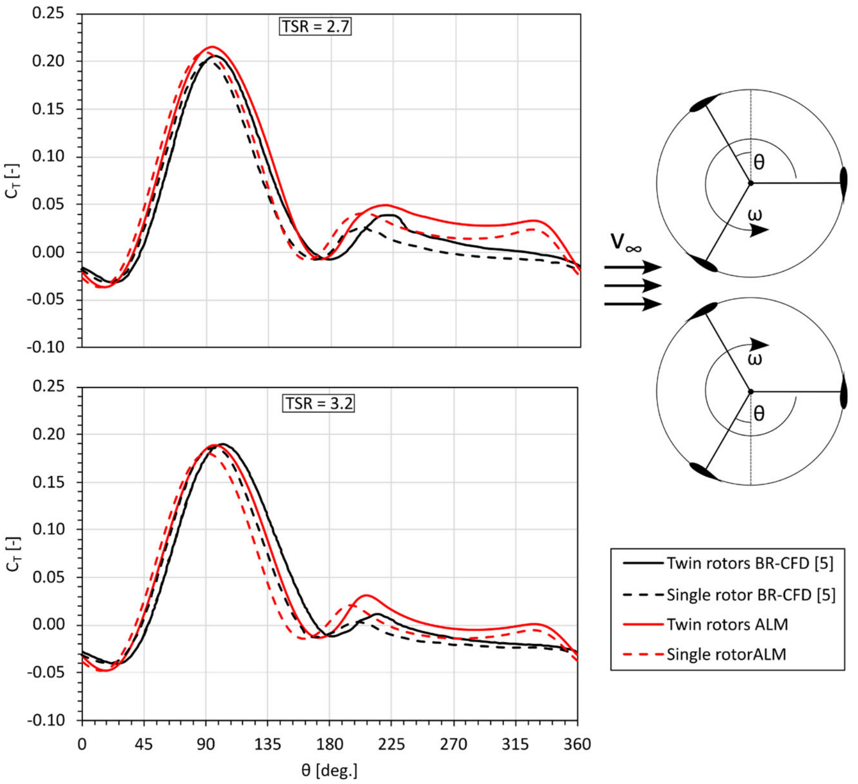

Figure 6 – Comparison between blade-resolved RANS [5] **and ALM in terms of torque coefficient for *3B-VAWT* twin rotors in the inward configuration at TSRs = 2.7 and 3.2.**

Figure 7 presents the same comparison for the outward configuration. The plot shows that during the first quarter of the azimuth angle range, where the interactions between adjacent blades are most significant ($0° \leq \theta \leq 90°$), the ALM torque coefficient trend showed a slight overestimation that increased gradually until reaching the peak torque near $\theta \approx 90°$, where the ALM was able to capture its azimuthal position but with an overestimated magnitude. Then the gap between the ALM torque and that of the reference data decreased gradually until matching at $\theta \approx 170°$. In the *downwind* azimuthal path on the other hand, torque production was overestimated along most of the path, as seen in the *inward* configuration. It is worth noticing that unlike in the *inward* configuration the ALM in the *outward* configuration accurately captured the trend of the torque coefficient without any shifts in the azimuth position.

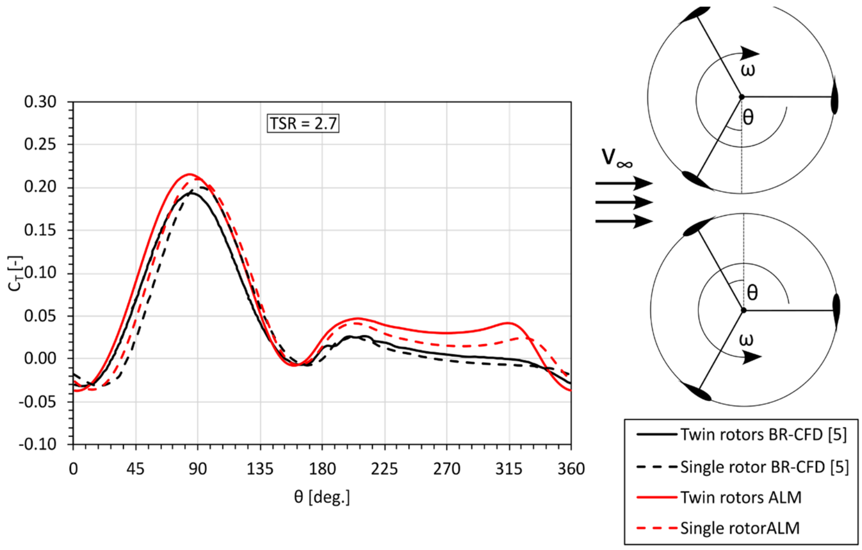

Figure 7 – Comparison between blade-resolved RANS [5] **and ALM in terms of torque coefficient for *3B-VAWT* twin rotors in the outward configuration at TSR = 2.7.**

4.1.2 Velocity profiles

In order to evaluate the ALM ability to reproduce the flow field around the twin rotors, the velocity profiles in the streamwise (*X*) and crosswise (*Y*) directions were compared between the ALM and the blade-resolved CFD from Zanforlin et al. [5]. For comparison, the velocity profile of the clockwise rotor was reoriented to the direction of the anticlockwise rotor, and an average was calculated for both rotors.

Figure 8 shows the velocity profiles sampled at TSRs 2.7 and 3.2 upstream of the twin rotor. At TSR = 2.7, it can be seen that the ALM shows good agreement with the blade-resolved CFD data, with some discrepancies in terms of: (i) *upwind* blockage effect, in particular the X-velocity deficit at the rotor centre (Y/D = 0); (ii) slope of variation of the Y-velocity, i.e., degree of expansion of the flow at the sides of the twin rotor and the gap. The same considerations can be made for TSR=3.2, but here the blockage effect induced by the twin rotor on the incoming flow is even more underpredicted with respect to blade-resolved CFD, both at the sides and in the gap.

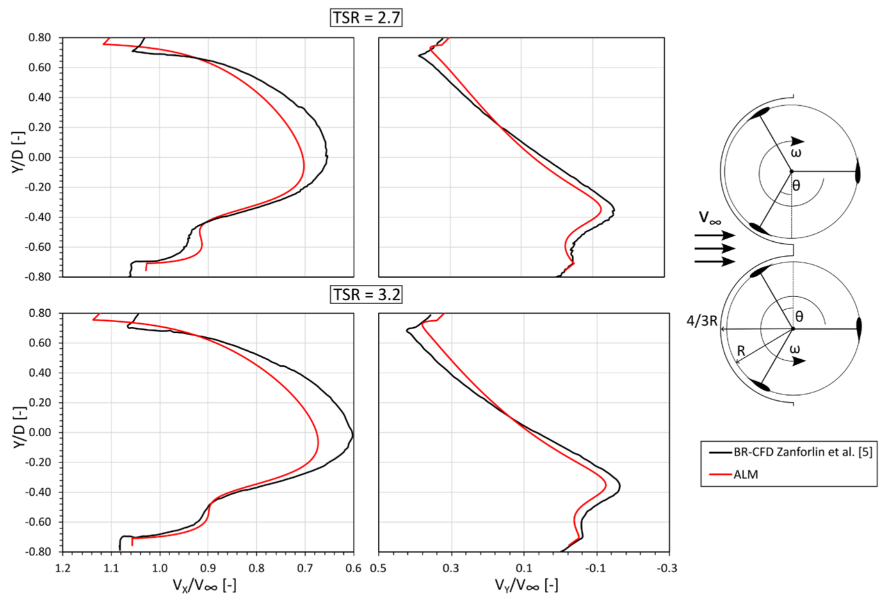

Figure 8 – Comparison between blade-resolved RANS [5] **and ALM in terms of upstream velocity profiles for *3B-VAWT* twin rotors at TSRs = 2.7 and 3.2.**

Based on previous considerations, it can be concluded that for the *3B-VAWT WindSpire* test case, the ALM is able not only to fairly reproduce the flow pattern induced by the pairing of multiple Darrieus rotors, which, according to Zanforlin et al. [5], consists in the suppression of the flow expansion in the mutual interaction area (Y/D < 0) of the rotors, but also to capture the corresponding enhancement of the torque production in the same region, with the following power augmentation effect. Nonetheless, two sources of discrepancy with respect to blade-resolved data can still be identified: (i) the low Reynolds numbers experienced by the blades (i.e., Re_c < 300k), which make the assessment of the input polar data extremely critical (see Section 3); (ii) the unsteady effects experienced by the blades could not be fully reproduced by the ALM whether through the use of Berg model or even without employing any dynamic stall model. The latter is more evident from the overestimation of the torque coefficient profile during the downwind azimuth positions observed for both inward and outward configurations and different TSRs. This observation aligns with a previous study for a stand-alone rotor [22].

4.2 Two-blade hydrokinetic turbine

In this section, the ALM results for the *2B-VAHT inward* counter-rotating twin rotors (see Section 2) are presented and compared to the blade-resolved CFD simulations from [29] for two different TSRs (2.5 and 3). In contrast with the *3B-VAWT* case, complete flow data were available for this turbine, enabling the advanced post-processing of the rotor flow via *LineAverage* sampling of the blade angle of attack, useful for a benchmarking of the ALM in terms of aerodynamic coefficients, and POD analysis of the wake.

4.2.1 Blade loading

Figure 9 shows the cyclic average power coefficient C_P computed using blade-resolved CFD and ALM for both stand-alone rotor and twin rotors of *2B-VAHT* at TSRs 2.5 and 3. In general, it can be observed that the ALM overestimates the average C_P in all cases. This overestimation is less prominent at TSR = 3 compared to TSR = 2.5.

However, the average value could hide significant differences in the instantaneous torque values, which could have been compensated during the averaging process along one rotor revolution. To take that into consideration, Figure 10 reports the comparison between ALM and CFD in terms of instantaneous C_T along one rotor revolution, for both the stand-alone and the twin rotor. At TSR = 2.5, the ALM was able to reproduce the torque profile in the whole *pitch-up* phase (0° < θ < 90°), up to its peak value for both single and twin rotors. In the *pitch-down* phase (90° < θ < 180°) instead, the ALM tends to underpredict torque production in both stand-alone and twin configurations. The opposite trend is observed in the *downwind* region (180° < θ < 360°), where the ALM overpredicts the blade loads with respect to reference data along the whole blade path. This behaviour is even more accentuated at TSR = 3, where, for both stand-alone and twin configurations, the ALM also anticipates the position of the torque peak of ca. 10°.

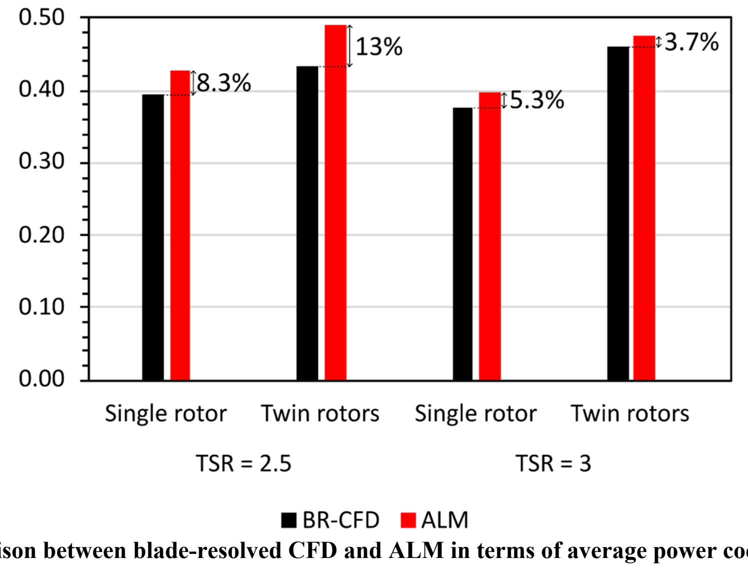

Figure 9 – Comparison between blade-resolved CFD and ALM in terms of average power coefficient 2B-VAHT single and twin rotors at TSRs 2.5 and 3.

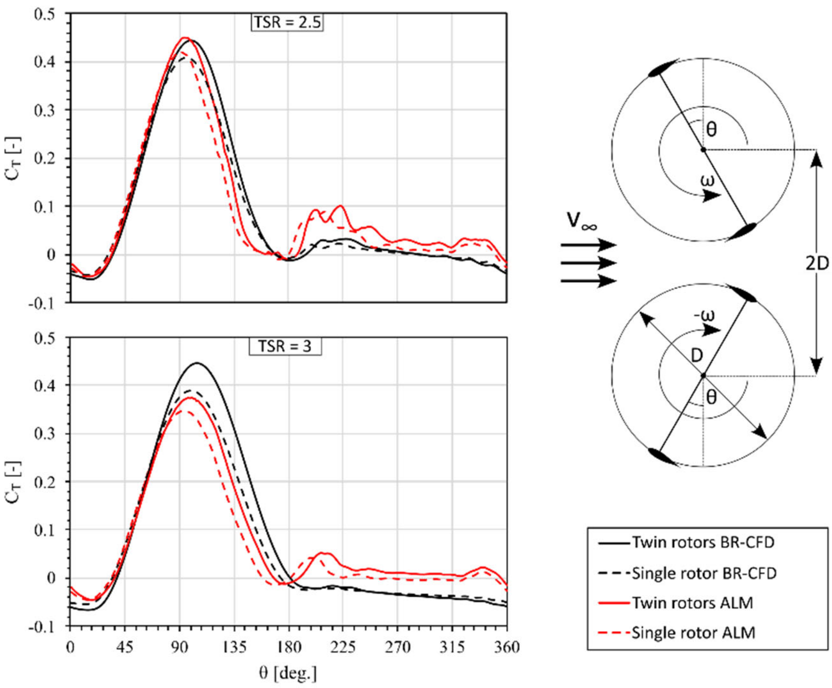

Figure 10 – Comparison between blade-resolved CFD and ALM in terms of instantaneous torque coefficient for *2B-VAHT* single and twin rotors at TSRs 2.5 and 3.

4.2.2 Blade kinematics

In order to gain a better insight into the discrepancies in terms of loads observed between ALM and blade-resolved CFD in Section 4.21, Figure 11 presents a similar comparison, but focusing on the local instantaneous angle of attack AoA and lift coefficient C_L. It is worth noting that the AoA was sampled using the same *LineAverage* technique for both ALM and blade-resolved CFD, with the settings described in Section 3.

For both TSRs, the trend of AoA variation predicted by the ALM show good agreement with that of the blade-resolved CFD, particularly at TSR = 3, exception made for a slight mismatch around θ ≈ 200°. More importantly, the ALM captures the increase in the AoA induced in the gap region (90° < θ < 225°) by the rotors' mutual interaction. This provides a first confirmation of what already observed for the *2B-VAWT* turbine (see Section 4.1.2), i.e., that the ALM in the present formulation is able to reproduce with sufficient accuracy the flow pattern generated by a twin rotor configuration.

The discrepancy in terms of blade loads highlighted in Section 4.2.1 must therefore be related to their computation inside the ALM algorithm, in particular the selected model for unsteady aerodynamics and dynamic stall. This in clearly visible in the C_L profiles reported in Figure 10. For TSR = 2.5, there is a good matching in terms of lift slope and stall delay between the two approaches, up to the maximum angle of attack (AoA ~ -17°). In the *pitch-down* phase nonetheless, where most of the power augmentation effect takes place in the twin rotor case, the Berg dynamic stall model tends to overestimate the amplitude of the lift hysteresis loop (-17° < AoA < -5°), underestimating in turn the corresponding torque production (see Figure 8). The opposite occurs in the *downwind* part, where the ALM keeps following a linear behaviour, while in the reference data there is both a reduction of the nominal slope and a lag of the instantaneous lift with respect to the angle of attack. This phenomenon is coherent with the airfoil behaviour observed during highly unsteady attached flow (as the one modelled in the theory of Theodorsen [49] for instance), and it is not included in the adopted Berg model. More advanced formulations are therefore required in the future. The weight of such unsteady loading, together with the discrepancy between ALM and blade-resolved CFD, is enhanced at TSR = 3, as separation-related effects lose importance.

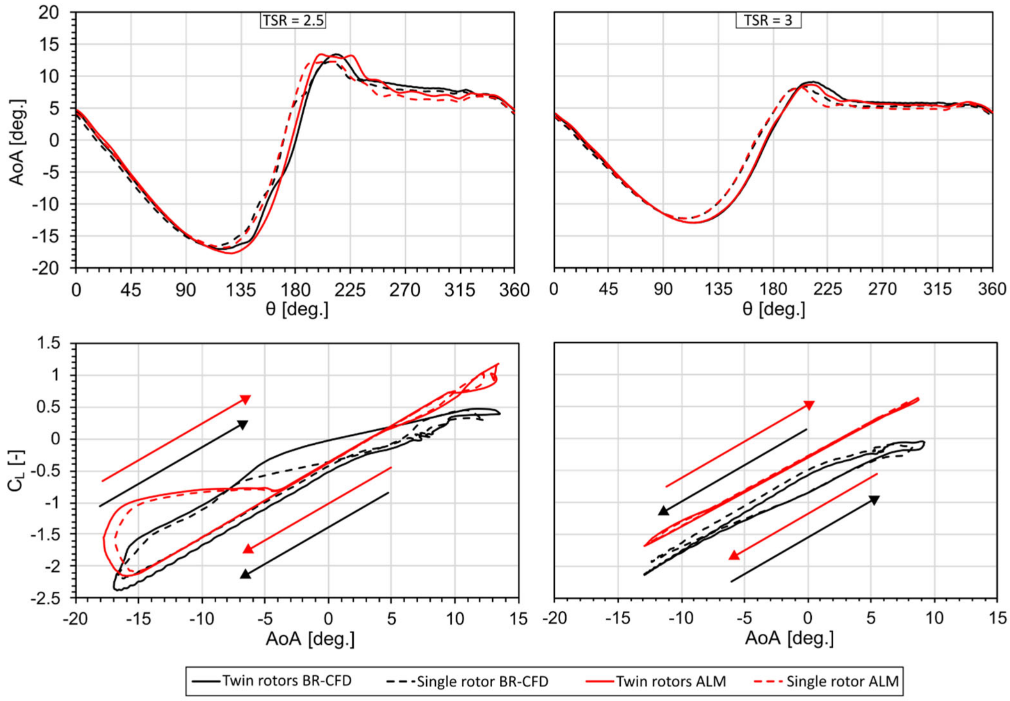

Figure 11 – Comparison between blade-resolved CFD and ALM in terms of AoA and lift hysteresis loop for *2B-VAHT* single and twin rotors at TSRs = 2.5 and 3.

4.2.3 Wake flow field

Figure 12 presents a comparison of the non-dimensional velocity profiles, V/V_∞, at various distances downstream of the rotors (1D, 3D, and 5D) obtained from ALM, Frozen ALM, and blade-resolved CFD simulations at TSRs 2.5 and 3. Overall, the velocity profiles of the ALM demonstrate good agreement with the reference profiles across all operating conditions. At TSR = 2.5, the ALM slightly overestimates the flow speed at the turbine sides ($Y/D \leq -2$ and $2 \leq Y/D$), while achieving a perfect match at TSR = 3. The presence of rotor-induced velocity deficits is accurately captured by the ALM for both TSRs, although the near wake velocity profile exhibits some variability at TSR = 2.5 and greater stability at TSR = 3. Within the mutual interaction region ($-0.5 \leq Y/D \leq 0.5$) at 1D and 3D, the ALM successfully captures the velocity variation, with minor differences compared to the blade-resolved CFD at TSR = 3. However, at 5D, the ALM solutions tend to overestimate the streamwise wake velocity between the rotors for both TSRs. Regarding the *Frozen ALM*, the velocity profiles closely match those of the blade-resolved CFD at the turbine leeward side ($Y/D < -1.5$ and $Y/D > 1.5$) at both TSRs. Although slight deviations are observed within the mutual interaction region, particularly near the rotors at X/D = 1 at TSR = 2.5.

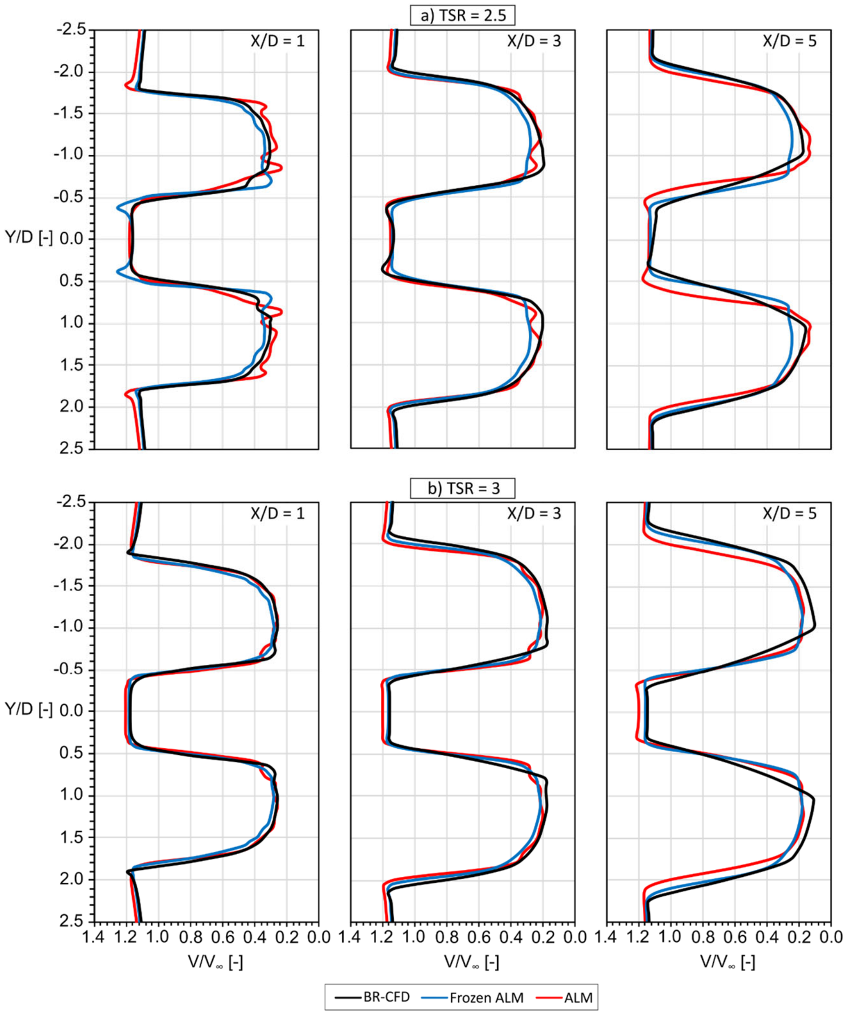

Figure 12 – Comparison between blade-resolved CFD and ALM at θ = 0° in terms of wake velocity profiles sampled at X/D = 1D, 3D, and 5D for *2B-VAHT* twin rotors at TSRs = a) 2.5 and b) 3 at θ = 0°.

Figures 13 and 15 depict the dimensionless vorticity contours obtained from the ALM, Frozen ALM, and blade-resolved CFD solutions at TSRs 2.5 and 3. It is apparent that in all cases and at both TSRs, the twin rotors produce symmetrical four vorticity sheets, each exhibiting varying directions due to the counter-rotating configuration. Each rotor generates two distinct shedding vortices which detach from the airfoil surface when subjected to a shift in the angle of attack sign. To analyze the evolution of these sheets, they were categorized as windward and leeward sheets. At each side, two vortices were identified and denoted as *W1* and *W2* for the windward vortices, and *L1* and *L2* for the leeward vortices. It is important to note that the identified vortices are generated by the same blade and correspond to two subsequent revolutions, while the ones in between have been generated by the other blade.

At TSR = 2.5, *W1* initiates at θ = 90° with a consistent slender structure across all cases. It gradually transforms into an elliptical shape until reaching θ = 360°, where the *W1* vortices of the blade-resolved CFD, *Frozen ALM*, and ALM simulations coincide at X/D ≈ 1. However, it is evident that the ALM vortex appears more compact compared to those of the Frozen ALM and blade-resolved CFD. This disparity becomes more pronounced from *W2*, being located at X/D ≈ 1.2 at θ = 90° and subsequently progressing to X/D ≈ 2 at θ = 360° in all simulations. Despite the similarity in shape and transport velocities between the windward vortices in all cases, their dissipation is different, especially at X/D ≈ 3. In the case of ALM, the dissipation of the windward vortices assumes a slender form with a higher vorticity magnitude. Conversely, the windward vortices of the blade-resolved CFD exhibit a wider, diffused shape with a lower vorticity magnitude. Interestingly, the Frozen ALM initially displays windward vortices similar to those of the blade-resolved CFD until approximately X/D ≈ 4, after which it demonstrates distinct dissipation behavior.

Regarding the leeward vortices at TSR = 2.5, it is apparent that their structures differ across all simulations from the initiation phase. This disparity can be attributed to two primary reasons. Firstly, there are discrepancies in the ALM load estimation at $\theta > 100°$ (see Fig. 10), which is the azimuthal region where these vortices are formed. Secondly, the projection of forces, which the ALM is inherently unable to reproduce, particularly those formed around the blade wall in the blade-resolved CFD case. The latter is depicted in detail in Figure 14. In the blade-resolved CFD results, due to the dynamic unsteadiness, a separation bubble is formed on the trailing edge, extending up to almost half of the airfoil surface. This results in the formation of four vortices in each half cycle. At $\theta = 90°$, around *L1*, there are two additional blue vortices alongside a counter-rotating red vortex. These vortices are not transported at the same speed, and this disparity becomes more pronounced at $\theta = 180°$ when *L1* and its accompanying counter-rotating vortex interact with another vortex from the previous cycle, gradually dissipating the counter-rotating vortex. This phenomenon is more clearly visible with *L2*, where at $\theta = 90°$ it pairs with another co-rotating vortex, leading to the complete disappearance of the counter-rotating vortex at $\theta = 270°$. Subsequently, these vortices interact to form a larger single vortex, which eventually dissipates, forming a thick layer of flow with a low vorticity magnitude.

In the case of the *Frozen ALM*, despite projecting the force magnitudes from the blade-resolved CFD case, the resulting vortical structures differ due to the different distribution of these forces when projected. In the *Frozen ALM*, the forces take on a circular shape. On the other hand, the ALM generates a leeward street with more concentrated circular-shaped vortices. These vortices maintain their shape until $X/D \approx 5$, where they slow down and pair with each other, leading to their dissipation along with the windward sheet. It is important to note that in both ALM and blade-resolved CFD simulations, the leeward vortices pair together, forming larger vortices. However, the location of these pairings differs between the simulations: $1 < X/D < 2$ for the blade-resolved CFD and $4 < X/D < 5$ for the ALM. In contrast, no vortex pairing occurs in the *Frozen ALM* case.

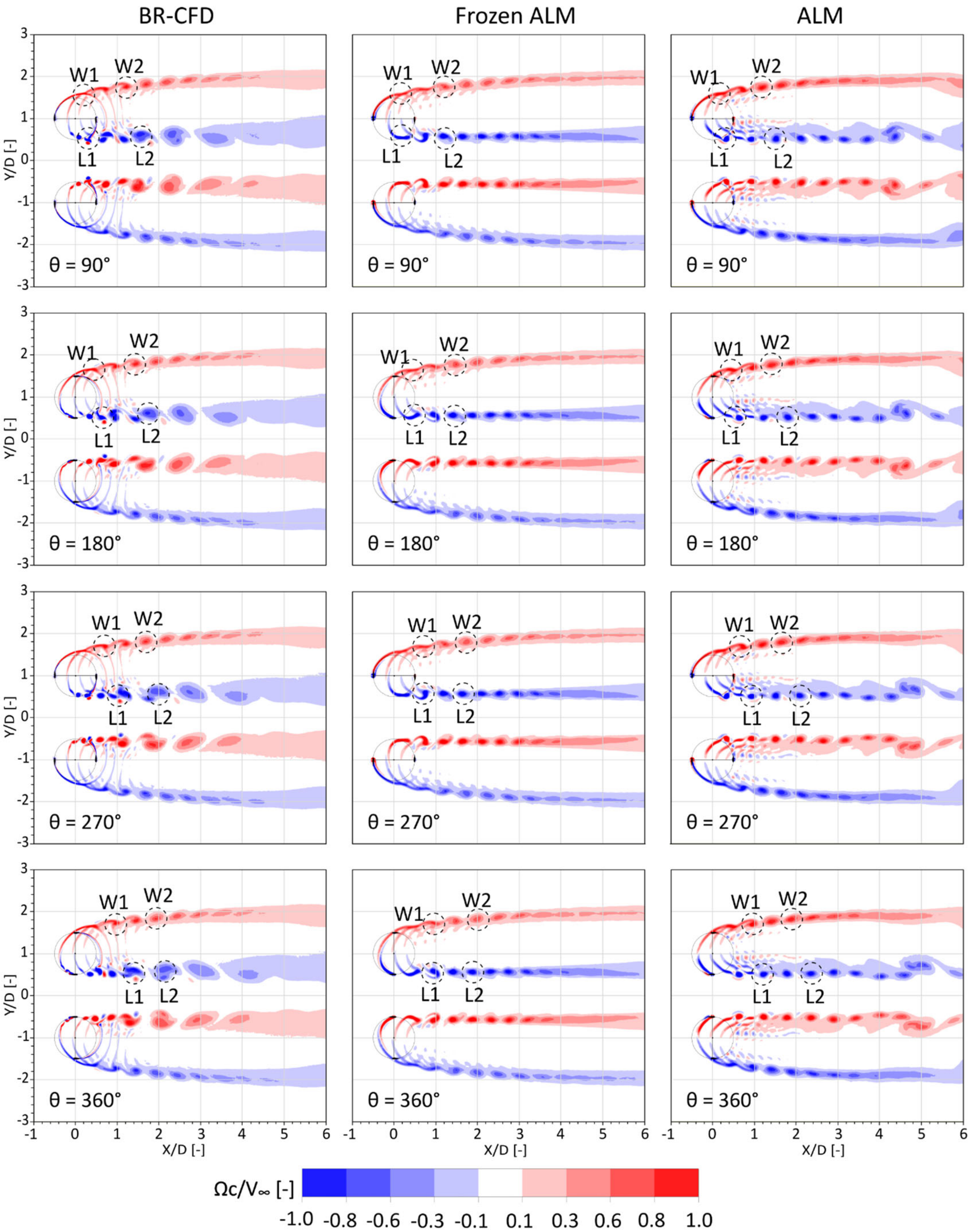

Figure 13 – Comparison between blade-resolved CFD and ALM at θ = 90°, 180°, 270°, and 360° in terms of dimensionless vorticity for *2B-VAHT* twin rotors at TSR = 2.5.

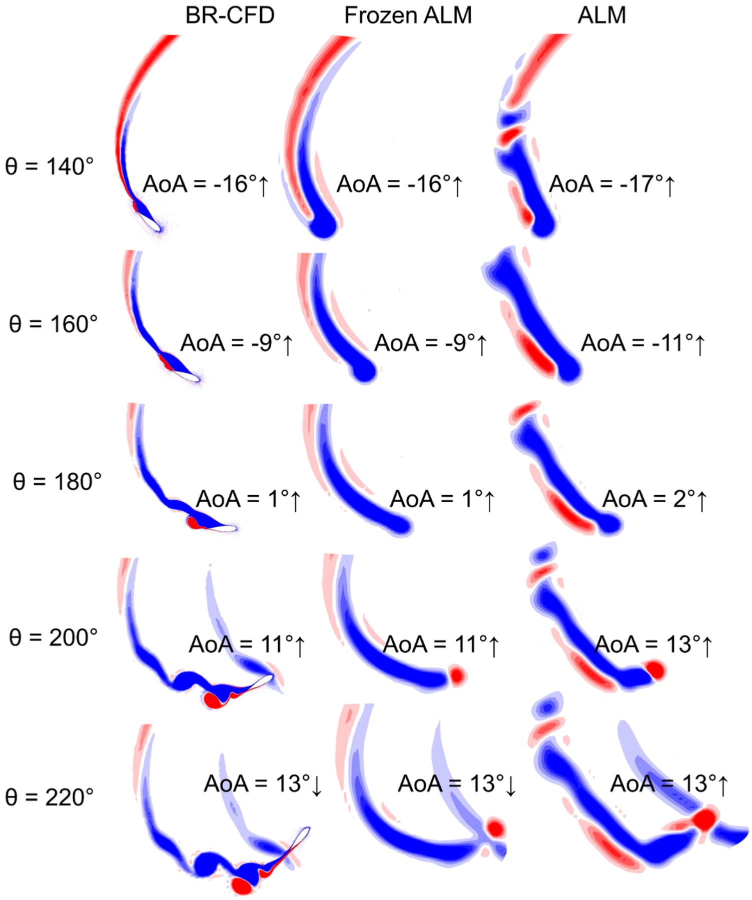

Figure 14 – Leeward vortex initiation for blade-resolved CFD compared with that of the Frozen ALM and ALM at TSR = 2.5.

At TSR = 3, the windward vortices look similar to those of TSR = 2.5 for all cases, with a single vortex produced every half cycle and a more compact structure for the ALM. The dissipation behavior is similar for all cases, with the ALM and *Frozen ALM* forming a thin layer of high vorticity flow that only in the ALM case, they break down into larger vortices upon interacting with the leeward street, more apparent at X/D > 7. In contrast, the blade-resolved CFD produces a thicker and more diffused windward street. Regarding the leeward vortices, due to the low angle of attack variation range at this TSR (see Fig. 9), the vortical structures formed on that side seem simpler compared to those at TSR = 2.5, with only a single vortex formed each half cycle, which quickly dissipates as shown from *L2* at θ = 360°. However, as noted before, due to the poor load estimation at θ > 70° (see Fig. 8), the leeward streets produced by the ALM have a completely different shape and concentration compared to those of the blade-resolved CFD and *Frozen ALM*, leading to different recovery behavior, which is more prominent at X/D ≈ 6.

To summarize, the proposed tool is able to reproduce the main features of the wake flow field in a fairly accurate manner. However, the ALM shows a slower diffusion in the windward vortex streets at both TSRs. This can be mainly attributed to the discrepancies in the load estimation that the ALM produces during the blade pitch down phase. It is important to note that this has also been observed in [22] for a stand-alone rotor. Based on the analysis above, the POD region was chosen to be within a streamwise distance of 1 ≤ X/D ≤ 5, since beyond this range, it is already evident that the flow behaves completely differently in both simulations.

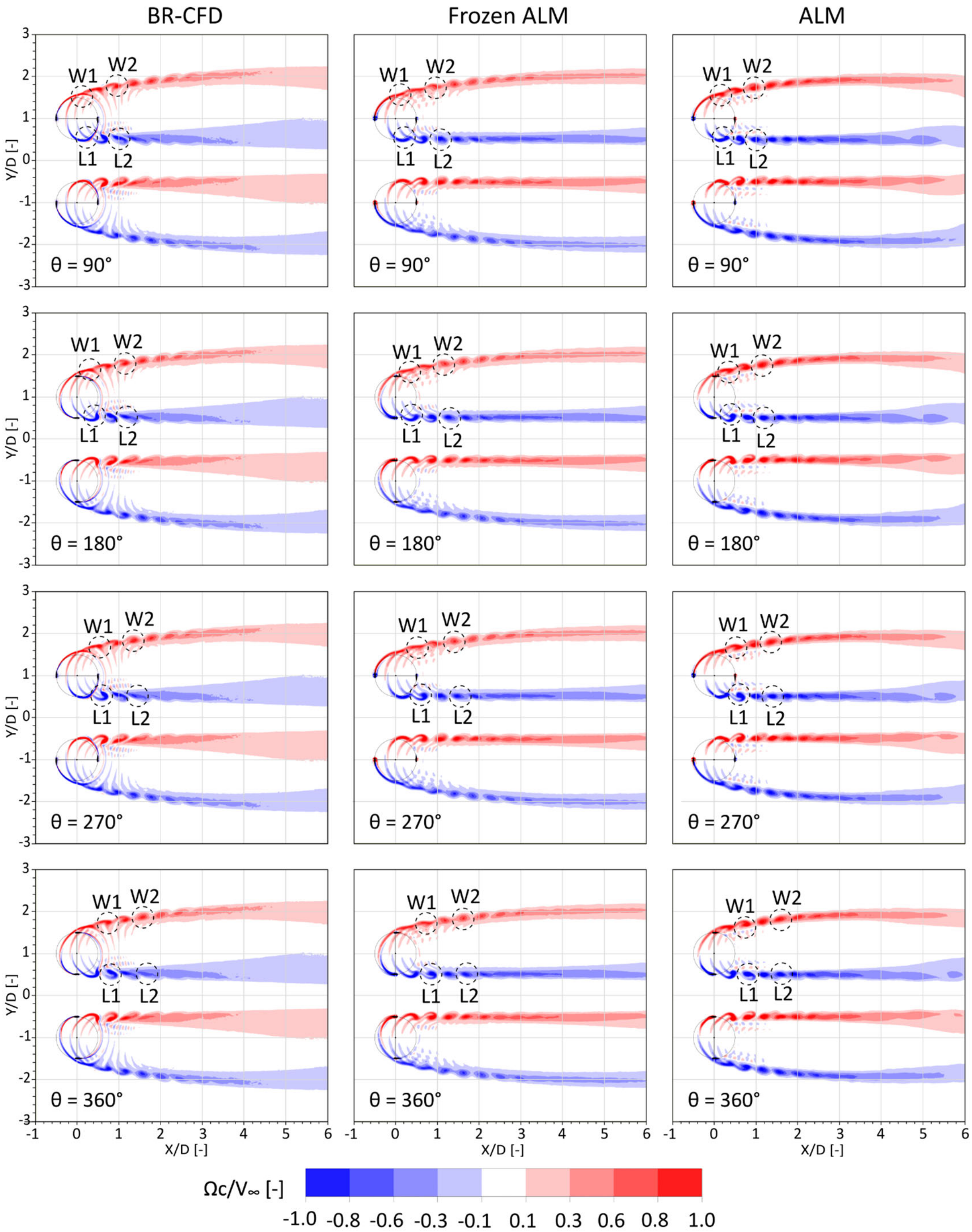

Figure 15 – Comparison between blade-resolved CFD and ALM at θ = 90°, 180°, 270°, and 360° in terms of dimensionless vorticity for *2B-VAHT* twin rotors at TSR = 3.

Figure 16 presents a comparison of the percentage of the POD modal energy captured by each spatial mode, as well as the cumulative total energy captured up to each mode, at two different TSRs of 2.5 and 3, calculated as explained in Section 3.4. At TSR = 2.5, the ALM simulation required 8 modes to capture over 90% of the total energy, while only 2 and 5 modes were needed in the case of Frozen ALM and blade-resolved CFD, respectively. At TSR = 3, due to the reduced influence of unsteady effects, more energy was captured by fewer modes in all simulations. Notably, the Frozen ALM and blade-resolved CFD exhibited a close match, with the first two modes capturing 96% and 94% of the total modal energy, respectively. In contrast, for the ALM, the first two modes accounted for only 67% of the total energy. These differences in the distribution of flow modal energy among the various modes between the ALM and blade-resolved CFD can be better understood by examining the corresponding modal spatial patterns.

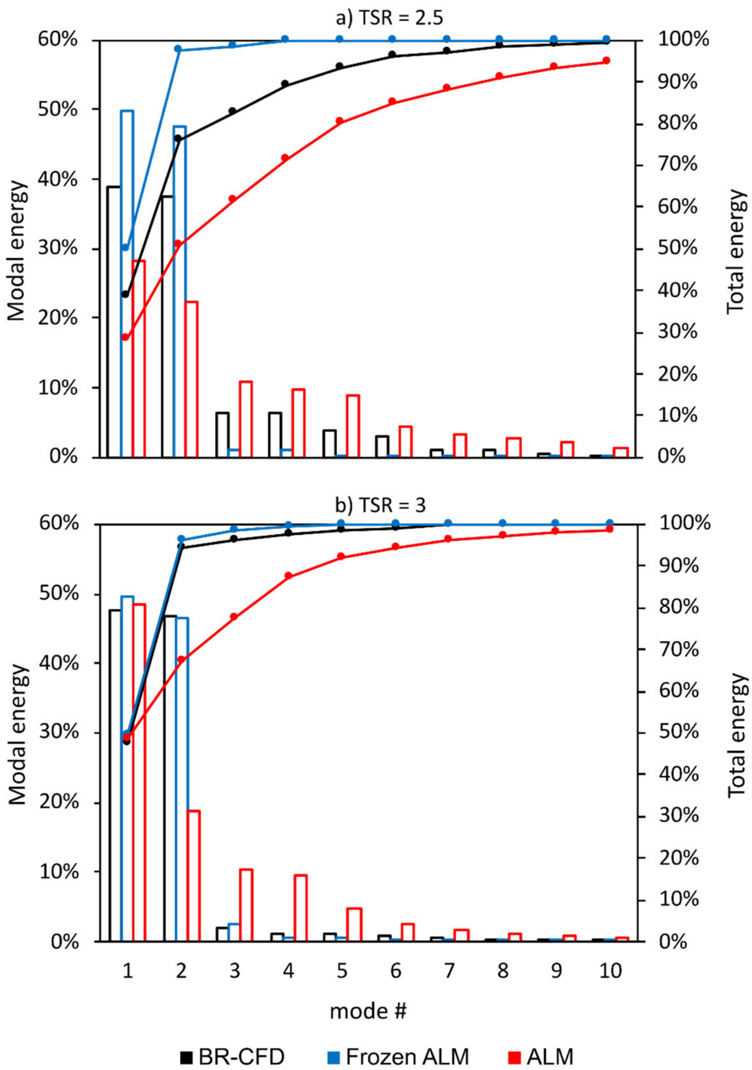

Figure 16 - Comparison between the percentage of modal energy for the ALM and blade-resolved CFD at TSRs a) 2.5 and b) 3.

Figure 17 illustrates the normalized mean velocity fields at TSR = 2.5 obtained through the three simulation techniques, along with the contour representing the mean velocity differences calculated by subtracting the mean velocity of the ALM fields from that of the blade-resolved CFD. Overall, the mean flow patterns reveal a considerable similarity in the distribution of the wake flow field, with only some noticeable differences highlighted by the mean velocity difference contour. A comparison between the Frozen ALM mean flow and the blade-resolved CFD demonstrates a close alignment in most regions, except for the wake borders where deviations occur. In contrast, the ALM mean flow exhibits greater acceleration in the area between the two rotors, as also observed in the velocity profiles presented in Figure 12.

The first four spatial modes resulted from the POD are shown in Fig. 18, offering further insights into the differences among the three simulations in terms of wake development at TSR = 2.5. Notably, the first four modes in all simulations exhibit a pattern where each pair of modes shows a spatial phase shift between them. This phenomenon has also been observed in a recent single rotor POD analysis conducted in [47]. In the case of blade-resolved CFD, the first two modes represent the dominant modes of velocity fluctuations resulting from the coupling of the windward streets, while the other pair captures the harmonics of these windward streets, featuring double the number of structures, along with structures associated with the leeward vortex streets. Conversely, as previously explained the Frozen ALM results do not exhibit this coupling between the windward vortices, despite projecting the same forces as in the blade-resolved CFD (see Fig. 13). This explains the absence of modes 1 and 2 from the

Frozen ALM modes, while modes 1 and 2 of the Frozen ALM align with modes 3 and 4 of the blade-resolved CFD.

Additionally, the first two modes of the ALM capture the fluctuations resulting from the pairing of the windward streets, where large structures are observed within 4 < X/D < 5, indicating the formation of a double-sized vortex due to an earlier pairing. It is important to note that the first two modes of both simulations are related to the convection of the windward streets. However, this represents a significant difference between the wake flow fields of the ALM and the blade-resolved CFD, as discussed earlier based on the vorticity flow field. On the other hand, the third and fourth modes of the ALM exhibit paired velocity fluctuation patterns arising from the shedding vortices near both the leeward and windward sides. From X/D = 1 up to X/D ≈ 3, modes 3 and 4 of the ALM exhibit strong similarities with modes 3 and 4 of the blade-resolved CFD, particularly in terms of the leeward streets.

Figure 19 displays the mean velocity contours for blade-resolved CFD, Frozen ALM, and ALM. as well as the mean velocity differences at TSR = 3. At this TSR, the mean flow in the ALM simulation shows greater acceleration than in the blade-resolved CFD on both the leeward and windward sides, which was previously observed in the velocity profiles shown in Fig. 12. The Frozen ALM, on the other hand, exhibits higher acceleration within the area of mutual interaction between the wakes of the two turbines at 2 < X/D < 4.

Figure 20 shows the initial four POD modes, the first two modes of both the blade-resolved CFD and the Frozen ALM show pairs of similar coherent structures with a streamwise phase shift, representing the velocity fluctuation pattern due to the shedding streets in both leeward and windward directions. The size and position of the coherent structures in the first two modes match well between the blade-resolved CFD and the Frozen ALM. For these two simulations, the 3rd mode shows a coherent pattern formed due to the dissipation of the leeward streets, while the 4th mode represents a breakdown of the first and second modes, showing double the number of coherent structures. At this TSR, the influence of the 3rd and 4th modes is marginal since the first two modes capture about 94% and 96% of the modal energy for the blade-resolved CFD and the Frozen ALM, respectively (see Fig. 16).

For the ALM, the first two modes represent a pair of coherent structures that are produced near the rotors due to the windward streets. The 3rd and 4th modes depict a breakdown of these windward structures in addition to those formed due to the leeward streets. Interestingly, the 3rd and 4th modes of the ALM show good agreement with the 1st and 2nd modes of the blade-resolved CFD and the Frozen ALM.

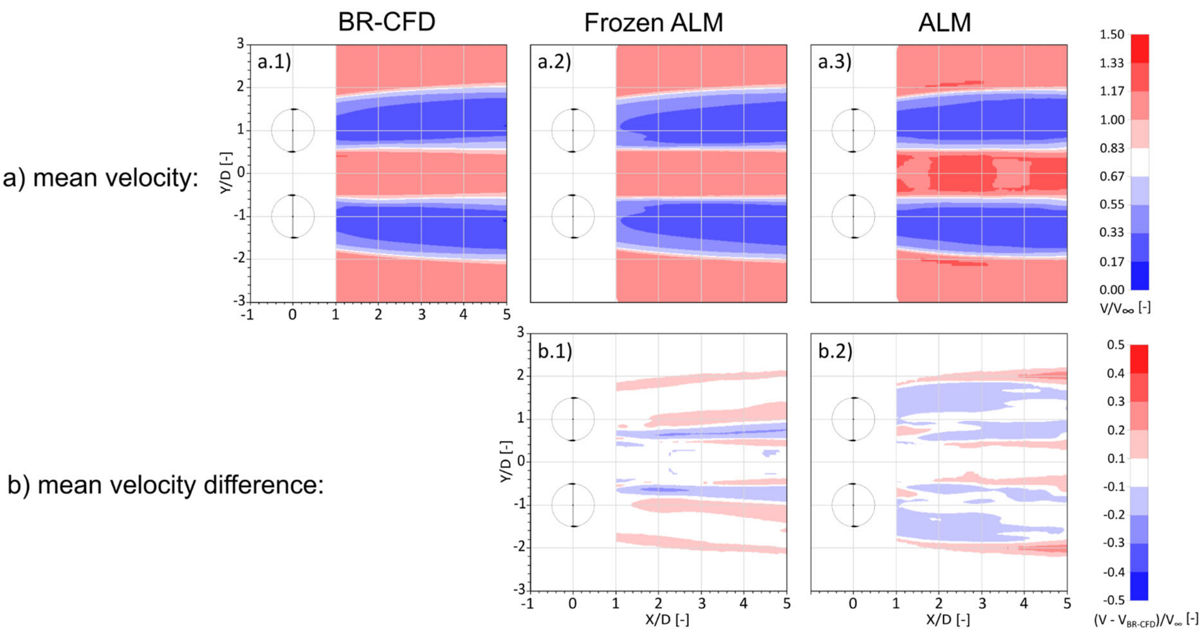

Figure 17 - Comparison between a) temporal mean of dimensionless velocity, b) mean velocity difference for *2B-VAHT* twin rotors at TSR = 2.5.

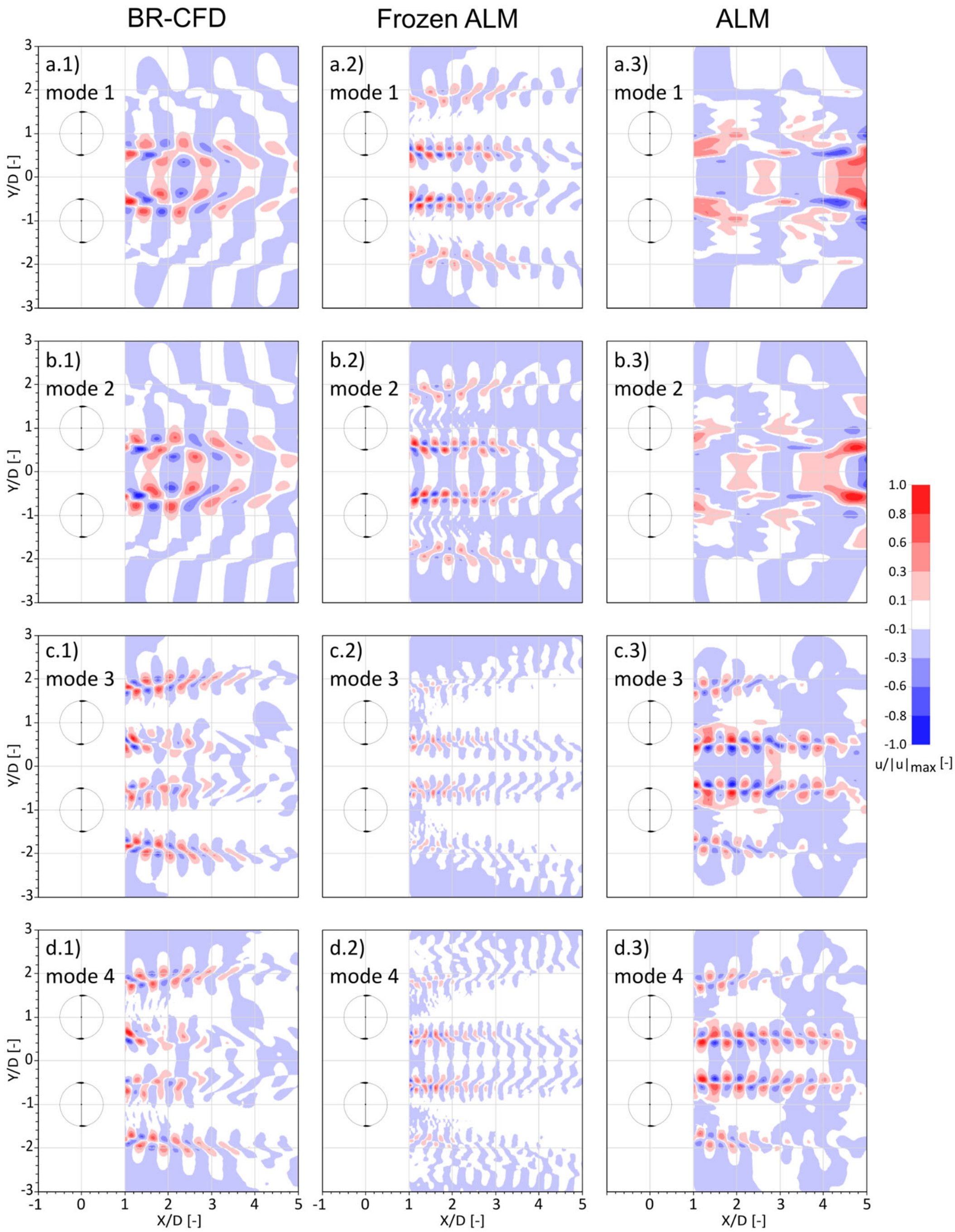

Figure 18 - Comparison between POD modes: a) mode 1, b) mode 2, c) mode 3, and d) mode 4 for *2B-VAHT* twin rotors at TSR = 2.5.

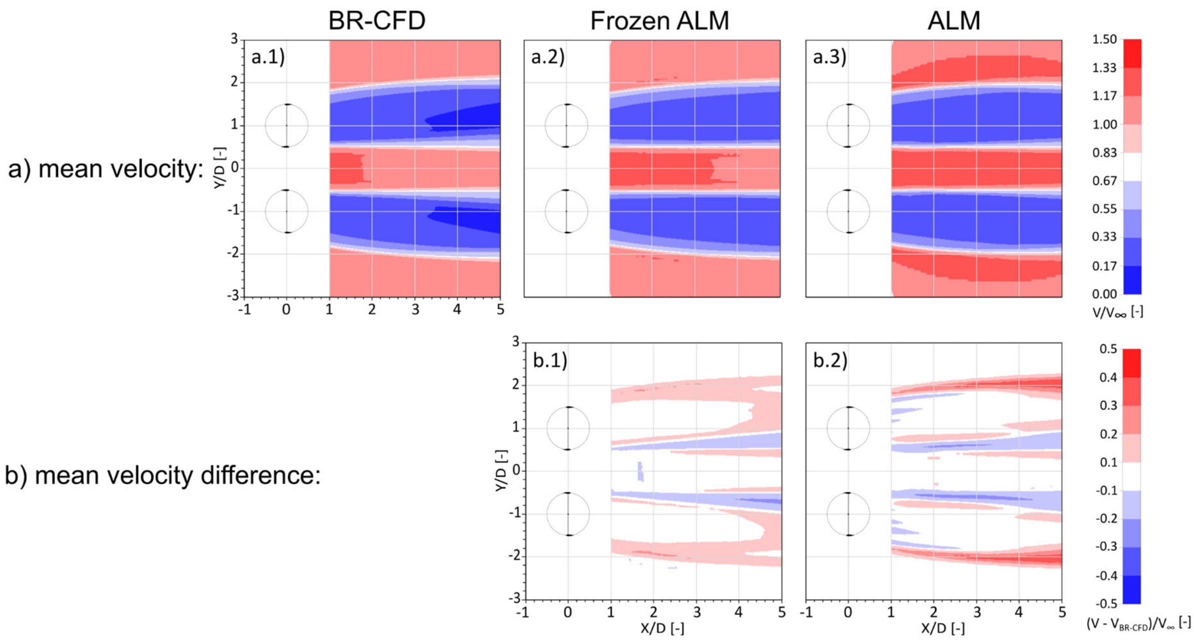

Figure 19 - Comparison between a) temporal mean of dimensionless velocity, b) mean velocity difference for *2B-VAHT* twin rotors at TSR = 3.

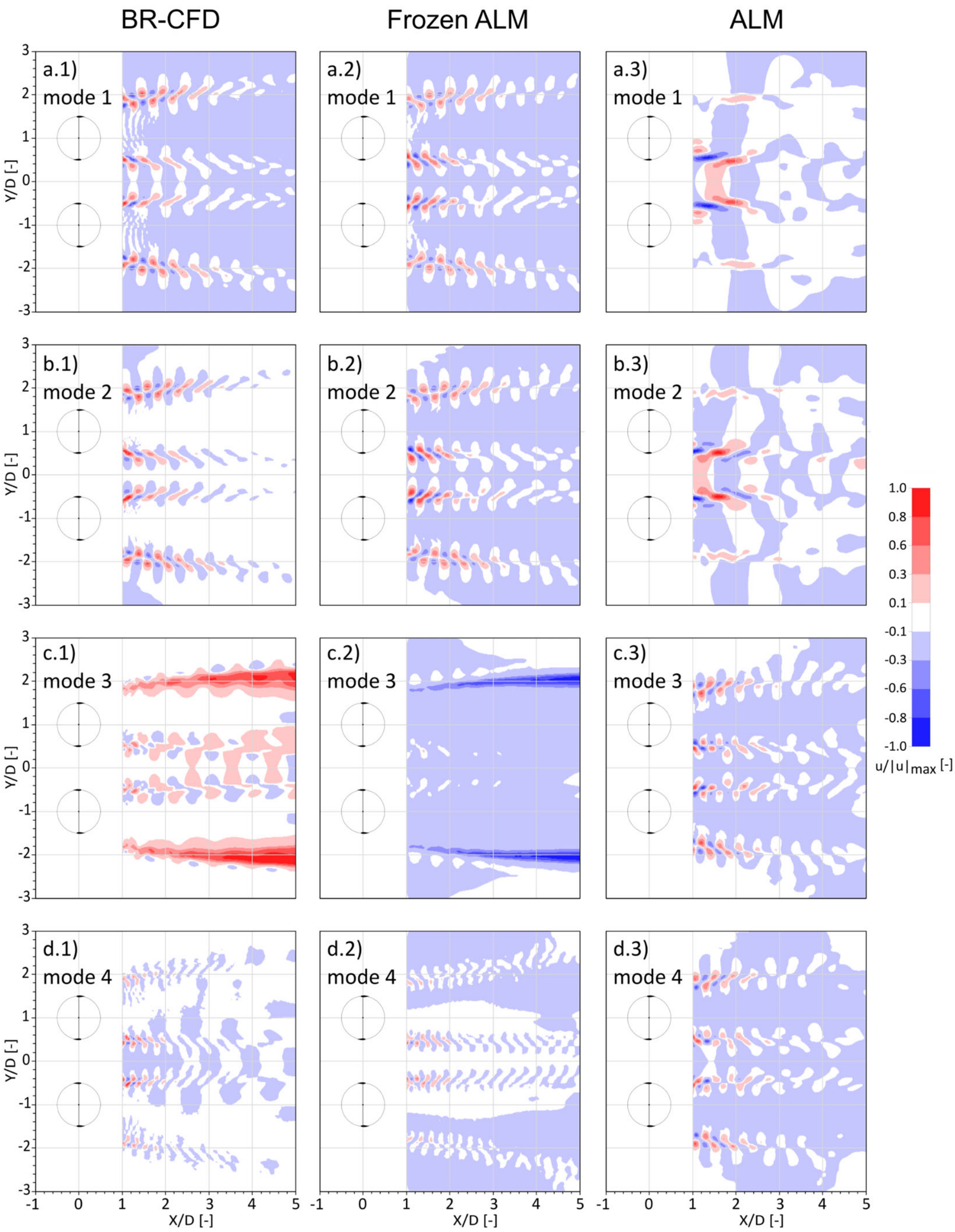

Figure 20 - Comparison between POD modes: a) mode 1, b) mode 2, c) mode 3, and d) mode 4 for *2B-VAHT* twin rotors at TSR = 3.

5. Discussion

In this study, the ALM simulation approach was thoroughly validated against blade-resolved CFD solutions to evaluate its potential in accurately predicting the performance of twin Darrieus turbines. The validation process focused on three key aspects: (i) estimation of the instantaneous turbine loads, (ii) ability to mimic the local flow kinematics, and (iii) reproduction of the wake behaviour.

The results from the validation campaign have highlighted that estimating the instantaneous blade load is a task that is highly dependent on the specific case, as previously mentioned in [22]. It is evident that this issue is not exclusive to the implementation of multiple rotors but is influenced by the geometric and operational characteristics of the turbines. Specifically, the analysis of the instantaneous torque coefficient results for the 3B-VAWT turbines indicated that the ALM consistently overestimated the torque coefficient during the downwind azimuthal path, although this discrepancy was less pronounced at higher tip speed ratios. Conversely, for the 2B-VAHK pair, this issue persisted even at higher tip speed ratios. The primary reason for this disparity can be attributed to the incapability of the Berg model to accurately capture the unsteady effects in the absence of dynamic stall. These unsteady effects may not have as significant an impact on the 3B-VAWT rotor due to differences in operational characteristics, such as the lower c/R ratio and the higher solidity.

In terms of the local variation of the flow field, which has been previously identified [29] as the primary source of efficiency improvement when two rotors are closely deployed, our findings reveal that the ALM successfully reproduces this effect. Although the data for the angle of attack was not available for the 3B-VAWT pair, we compared the velocity profiles in the vicinity of the blades with the results published by [5]. For the 2B-VAHT rotor pair, the AoA values generated by the ALM closely matched those obtained from the blade-resolved CFD simulations, particularly at higher TSR. These findings readily suggest that the ALM has the potential to be employed in multirotor configurations, as it can capture the corresponding array effects.

The comparative analysis using POD on the 2B-VAHT twin rotors revealed that the ALM simulation could effectively capture the main flow patterns shown by blade-resolved CFD, despite using different temporal and spatial discretisation's. The POD analysis played a crucial role in identifying the dominant flow patterns associated with the wake behind the twin rotors and highlighting the differences between the wakes produced by both simulations. In this context, the use of the *Frozen ALM* in the POD analysis allowed the distinction between the discrepancies due to the load estimation and those due to other factors such as the projection function. For instance, at high TSR, where the dynamic effects are minimal, the dominant modes of both blade-resolved CFD and Frozen ALM matches in terms of energy content as well as the coherent structures. Furthermore, the analysis clearly demonstrated that the discrepancies observed in the ALM reproduced wake were primarily due to the underestimation of the load generated during blade pitch down, which implicitly affected the wake recovery behavior.

Overall, the ALM has demonstrated exceptional capability in reproducing changes in local flow kinematics, which is essential for closely-spaced Darrieus turbine applications [29]. This has made it a suitable tool for interdisciplinary analyses of multiple Darrieus rotor problems, particularly for design and optimization purposes.

The spatial domain of the ALM is smaller than that of the blade-resolved CFD simulation (42D × 90D vs. 30D × 45D), with approximately 180k elements compared to 1,000k elements. Additionally, the ALM uses a larger $\Delta\theta$ (1°) than the blade-resolved CFD (0.4°), resulting in a significant reduction in computational time. The ALM takes approximately 7 core-hours per revolution, while the blade-resolved CFD takes around 508 core-hours per revolution.

6. Conclusions

This study has presented a comprehensive validation campaign of the ALM tool in its two-dimensional form for closely-spaced twin Darrieus turbines. Proving that this computationally-efficient method is able to capture the complex flow interactions, which have been to date analyzed only by means of blade-resolved CFD, is thought to represent a finding of particular relevance for industry, as this method can become the new standard in the growing sector, for example, of hydrokinetic turbines that need to be deployed into arrays.

The validation was conducted by comparing the results of the ALM with those of blade-resolved CFD simulations, and it aimed at assessing the ALM's ability to estimate the instantaneous turbine loads, mimic the local flow kinematics, and reproduce the wake behaviour. The validation campaign was carried out for two different pairs of Darrieus turbines: *3B-VAWT* and *2B-VAHT*, which exhibit different geometrical and operational characteristics.

The results of the validation campaign have demonstrated that the ALM is able of accurately reproducing the local flow kinematics, which is essential for closely-spaced Darrieus turbine applications. The load analysis showed that the ALM can capture the instantaneous load with good to fair accuracy, although this may be case-dependent due to the sensitivity of the adopted dynamic stall model to geometrical and operating conditions. The wake analysis conducted through performing POD analyses revealed that the main flow fluctuating patterns from the blade-resolved simulation are well captured by the ALM. In summary, the ALM requires much less computational resources compared to blade-resolved CFD for simulating a twin-rotor configuration, with a computational time difference of almost two orders of magnitude. This makes the ALM an attractive alternative for complicated and interdisciplinary applications, such as simulating the flow around a floating Darrieus wind turbine or examining the effect of Darrieus hydrokinetic turbines on a channel flow.

In future research, it would be beneficial to expand the validation of the ALM to encompass three-dimensional simulations with experimental validation. These simulations should consider factors such as tip losses and the impact of vertical mixing on wake recovery. Furthermore, incorporating additional physical phenomena into the ALM model would enhance our understanding of how these machines perform in realistic scenarios.

References

[1] W. Tjiu, T. Marnoto, S. Mat, M. H. Ruslan, and K. Sopian, 'Darrieus vertical axis wind turbine for power generation II: Challenges in HAWT and the opportunity of multi-megawatt Darrieus VAWT development', *Renewable Energy*, vol. 75, pp. 560–571, Mar. 2015, doi: 10.1016/j.renene.2014.10.039.

[2] V. F.-C. Rolin and F. Porté-Agel, 'Experimental investigation of vertical-axis wind-turbine wakes in boundary layer flow', *Renewable Energy*, vol. 118, pp. 1–13, Apr. 2018, doi: 10.1016/j.renene.2017.10.105.

[3] F. Balduzzi, P. F. Melani, G. Soraperra, A. Brighenti, L. Battisti, and A. Bianchini, 'Some design guidelines to adapt a Darrieus vertical axis turbine for use in hydrokinetic applications', *E3S Web Conf.*, vol. 312, p. 08017, 2021, doi: 10.1051/e3sconf/202131208017.

[4] J. O. Dabiri, 'Potential order-of-magnitude enhancement of wind farm power density via counter-rotating vertical-axis wind turbine arrays', *Journal of Renewable and Sustainable Energy*, vol. 3, no. 4, p. 043104, Jul. 2011, doi: 10.1063/1.3608170.

[5] S. Zanforlin and T. Nishino, 'Fluid dynamic mechanisms of enhanced power generation by closely spaced vertical axis wind turbines', *Renewable Energy*, vol. 99, pp. 1213–1226, Dec. 2016, doi: 10.1016/j.renene.2016.08.015.

[6] O. S. Mohamed, A. Ibrahim, and A. M. R. El Baz, 'CFD Investigation of the Multiple Rotors Darrieus Type Turbine Performance', presented at the ASME Turbo Expo 2019: Turbomachinery Technical Conference and Exposition, American Society of Mechanical Engineers Digital Collection, Nov. 2019. doi: 10.1115/GT2019-91491.

[7] A. S. Alexander and A. Santhanakrishnan, 'Mechanisms of power augmentation in two side-by-side vertical axis wind turbines', *Renewable Energy*, vol. 148, pp. 600–610, Apr. 2020, doi: 10.1016/j.renene.2019.10.149.

[8] H.-D. Zheng, X. Y. Zheng, and S. X. Zhao, 'Arrangement of clustered straight-bladed wind turbines', *Energy*, vol. 200, p. 117563, Jun. 2020, doi: 10.1016/j.energy.2020.117563.

[9] M. Guilbot, S. Barre, G. Balarac, C. Bonamy, and N. Guillaud, 'A numerical study of Vertical Axis Wind Turbine performances in twin-rotor configurations', *J. Phys.: Conf. Ser.*, vol. 1618, no. 5, p. 052012, Sep. 2020, doi: 10.1088/1742-6596/1618/5/052012.

[10] S. Sahebzadeh, A. Rezaeiha, and H. Montazeri, 'Vertical-axis wind-turbine farm design: Impact of rotor setting and relative arrangement on aerodynamic performance of double rotor arrays', *Energy Reports*, vol. 8, pp. 5793–5819, Nov. 2022, doi: 10.1016/j.egyr.2022.04.030.

[11] 'Comparison between two-dimensional and three-dimensional computational fluid dynamics techniques for two straight-bladed vertical-axis wind turbines in inline arrangement - Saeed Nazari, Mahdi Zamani, Sajad A Moshizi, 2018'. https://journals.sagepub.com/doi/10.1177/0309524X18780384 (accessed Jun. 30, 2022).

[12] S. Draper and T. Nishino, 'Centred and staggered arrangements of tidal turbines', *Journal of Fluid Mechanics*, vol. 739, pp. 72–93, Jan. 2014, doi: 10.1017/jfm.2013.593.

[13] T. Nishino and R. H. J. Willden, 'The efficiency of an array of tidal turbines partially blocking a wide channel', *J. Fluid Mech.*, vol. 708, pp. 596–606, Oct. 2012, doi: 10.1017/jfm.2012.349.

[14] D. D. Tavernier, C. Ferreira, A. Li, U. S. Paulsen, and H. A. Madsen, 'Towards the understanding of vertical-axis wind turbines in double-rotor configuration.', *J. Phys.: Conf. Ser.*, vol. 1037, no. 2, p. 022015, Jun. 2018, doi: 10.1088/1742-6596/1037/2/022015.

[15] O. Gauvin-Tremblay and G. Dumas, 'Hydrokinetic turbine array analysis and optimization integrating blockage effects and turbine-wake interactions', *Renewable Energy*, vol. 181, pp. 851–869, Jan. 2022, doi: 10.1016/j.renene.2021.09.003.

[16] J. N. Sorensen and W. Z. Shen, 'Numerical Modeling of Wind Turbine Wakes', *Journal of Fluids Engineering*, vol. 124, no. 2, pp. 393–399, May 2002, doi: 10.1115/1.1471361.

[17] S. Shamsoddin and F. Porté-Agel, 'Large Eddy Simulation of Vertical Axis Wind Turbine Wakes', *Energies*, vol. 7, no. 2, Art. no. 2, Feb. 2014, doi: 10.3390/en7020890.

[18] P. Bachant, A. Goude, and M. Wosnik, 'Actuator line modeling of vertical-axis turbines', *arXiv:1605.01449 [physics]*, Sep. 2018, Accessed: Jun. 16, 2020. [Online]. Available: http://arxiv.org/abs/1605.01449

[19] V. Mendoza, P. Bachant, C. Ferreira, and A. Goude, 'Near-wake flow simulation of a vertical axis turbine using an actuator line model', *Wind Energy*, vol. 22, no. 2, pp. 171–188, 2019, doi: 10.1002/we.2277.

[20] P. F. Melani, F. Balduzzi, G. Ferrara, and A. Bianchini, 'Tailoring the actuator line theory to the simulation of Vertical-Axis Wind Turbines', *Energy Conversion and Management*, vol. 243, p. 114422, Sep. 2021, doi: 10.1016/j.enconman.2021.114422.

[21] P. F. Melani, F. Balduzzi, G. Ferrara, and A. Bianchini, 'Development of a desmodromic variable pitch system for hydrokinetic turbines', *Energy Conversion and Management*, vol. 250, p. 114890, Dec. 2021, doi: 10.1016/j.enconman.2021.114890.

[22] O. S. Mohamed, P. F. Melani, F. Balduzzi, G. Ferrara, and A. Bianchini, 'An insight on the key factors influencing the accuracy of the actuator line method for use in vertical-axis turbines: Limitations and open challenges', *Energy Conversion and Management*, vol. 270, p. 116249, Oct. 2022, doi: 10.1016/j.enconman.2022.116249.

[23] S. H. Hezaveh, E. Bou-Zeid, J. Dabiri, M. Kinzel, G. Cortina, and L. Martinelli, 'Increasing the Power Production of Vertical-Axis Wind-Turbine Farms Using Synergistic Clustering', *Boundary-Layer Meteorol*, vol. 169, no. 2, pp. 275–296, Nov. 2018, doi: 10.1007/s10546-018-0368-0.

[24] S. R. V, R. S. Solanki, V. K. Chalamalla, and S. S. Sinha, 'Numerical simulations and analysis of flow past vertical-axis wind turbines employing the actuator line method', presented at the Proceedings of the 26thNational and 4th International ISHMT-ASTFE Heat and Mass Transfer Conference December 17-20, 2021, IIT Madras, Chennai-600036, Tamil Nadu, India, Begel House Inc., 2021. doi: 10.1615/IHMTC-2021.4110.

[25] J. H. Zhang, F.-S. Lien, and E. Yee, 'Investigations of Vertical-Axis Wind-Turbine Group Synergy Using an Actuator Line Model', *Energies*, vol. 15, no. 17, Art. no. 17, Jan. 2022, doi: 10.3390/en15176211.

[26] P. F. Melani, F. Balduzzi, and A. Bianchini, 'A Robust Procedure to Implement Dynamic Stall Models Into Actuator Line Methods for the Simulation of Vertical-Axis Wind Turbines', *Journal of Engineering for Gas Turbines and Power*, vol. 143, no. 11, Sep. 2021, doi: 10.1115/1.4051909.

[27] P. F. Melani, F. Balduzzi, G. Ferrara, and A. Bianchini, 'How to extract the angle attack on airfoils in cycloidal motion from a flow field solved with computational fluid dynamics? Development and verification of a robust computational procedure', *Energy Conversion and Management*, vol. 223, p. 113284, Nov. 2020, doi: 10.1016/j.enconman.2020.113284.

[28] O. S. Mohamed, A. M. R. Elbaz, and A. Bianchini, 'A better insight on physics involved in the self-starting of a straight-blade Darrieus wind turbine by means of two-dimensional Computational Fluid Dynamics',

Journal of Wind Engineering and Industrial Aerodynamics, vol. 218, p. 104793, Nov. 2021, doi: 10.1016/j.jweia.2021.104793.

[29] O. S. Mohamed, P. F. Melani, F. Balduzzi, G. Ferrara, and A. Bianchini, 'An insight on the physical mechanisms responsible of power augmentation in a pair of counter-rotating Darrieus turbines', *Energy Conversion and Management*, vol. 284, p. 116991, May 2023, doi: 10.1016/j.enconman.2023.116991.

[30] E. Jost, L. Klein, H. Leipprand, T. Lutz, and E. Krämer, 'Extracting the angle of attack on rotor blades from CFD simulations', *Wind Energy*, vol. 21, no. 10, pp. 807–822, 2018, doi: 10.1002/we.2196.

[31] L. N. Azadani, 'Vertical axis wind turbines in cluster configurations', *Ocean Engineering*, vol. 272, p. 113855, Mar. 2023, doi: 10.1016/j.oceaneng.2023.113855.

[32] L. Cacciali, L. Battisti, and S. Dell'Anna, 'Multi-Array Design for Hydrokinetic Turbines in Hydropower Canals', *Energies*, vol. 16, no. 5, Art. no. 5, Jan. 2023, doi: 10.3390/en16052279.

[33] C. S. Ferreira, H. A. Madsen, M. Barone, B. Roscher, P. Deglaire, and I. Arduin, 'Comparison of aerodynamic models for Vertical Axis Wind Turbines', *J. Phys.: Conf. Ser.*, vol. 524, p. 012125, Jun. 2014, doi: 10.1088/1742-6596/524/1/012125.

[34] C. de Boor, *A Practical Guide to Splines*. in Applied Mathematical Sciences. New York: Springer-Verlag, 1978. Accessed: Nov. 23, 2020. [Online]. Available: https://www.springer.com/gp/book/9780387953663

[35] P. G. Migliore, W. P. Wolfe, and J. B. Fanucci, 'Flow Curvature Effects On Darrieus Turbine Blade Aerodynamics', *Journal of energy*, vol. 4, no. 2, pp. 49–55, 1980, doi: 10.2514/3.62459.

[36] J. M. Rainbird *et al.*, 'On the influence of virtual camber effect on airfoil polars for use in simulations of Darrieus wind turbines', *Energy Conversion and Management*, vol. 106, pp. 373–384, Dec. 2015, doi: 10.1016/j.enconman.2015.09.053.

[37] M. Drela, 'XFOIL: An Analysis and Design System for Low Reynolds Number Airfoils', in *Conference on Low Reynolds Number Airfoil Aerodynamics*, University of Notre Dame, Jun. 1989. doi: 10.1007/978-3-642-84010-4_1.

[38] L. A. Viterna and D. C. Janetzke, 'Theoretical And Experimental Power From Large Horizontal-Axis Wind Turbines', *NASA Technical Memorandum*, 1982.

[39] D. Marten *et al.*, 'Effects of airfoil's polar data in the stall region on the estimation of Darrieus wind turbines performance', *J. Eng. Gas Turbines Power*, vol. 139, no. 2, pp. 022606–9, 2016, doi: 10.1115/1.4034326.

[40] B. Massé, 'Description de deux programmes d'ordinateur pour le calcul des performances et des charges aérodynamiques pour les éoliennes à axe vertical', technical report IREQ-2379, 1981.

[41] L. A. Martínez-Tossas, M. J. Churchfield, and C. Meneveau, 'Optimal smoothing length scale for actuator line models of wind turbine blades based on Gaussian body force distribution', *Wind Energy*, vol. 20, no. 6, pp. 1083–1096, 2017, doi: 10.1002/we.2081.

[42] F. R. Menter, 'Zonal Two Equation Kappa-Omega Turbulence Models for Aerodynamic Flows', presented at the AIAA Fluid Dynamics Conference, Orlando, FL, Jan. 1993. Accessed: Apr. 19, 2023. [Online]. Available: https://ntrs.nasa.gov/citations/19960044572

[43] F. Balduzzi, A. Bianchini, R. Maleci, G. Ferrara, and L. Ferrari, 'Critical issues in the CFD simulation of Darrieus wind turbines', *Renewable Energy*, vol. 85, pp. 419–435, 2016, doi: 10.1016/j.renene.2015.06.048.

[44] F. Balduzzi, A. Bianchini, G. Ferrara, and L. Ferrari, 'Dimensionless numbers for the assessment of mesh and timestep requirements in CFD simulations of Darrieus wind turbines', *Energy*, vol. 97, pp. 246–261, Feb. 2016, doi: 10.1016/j.energy.2015.12.111.

[45] P. F. Melani, P. Schito, and G. Persico, 'Experimental assessment of an ACL simulation tool for VAWTs', in *Proc. of the TUrbWind 2018 Colloquium*, Riva del Garda (Italy), September 6-7, 2018.

[46] K. Taira *et al.*, ‘Modal Analysis of Fluid Flows: An Overview’, *AIAA Journal*, vol. 55, no. 12, pp. 4013–4041, 2017, doi: 10.2514/1.J056060.

[47] L. Chen, J. Xu, and R. Dai, ‘Numerical prediction of switching gurney flap effects on straight bladed VAWT power performance’, *J Mech Sci Technol*, vol. 34, no. 12, pp. 4933–4940, Dec. 2020, doi: 10.1007/s12206-020-2106-z.

[48] A. Sheidani, S. Salavatidezfouli, G. Stabile, and G. Rozza, ‘Assessment of URANS and LES methods in predicting wake shed behind a vertical axis wind turbine’, *Journal of Wind Engineering and Industrial Aerodynamics*, vol. 232, p. 105285, Jan. 2023, doi: 10.1016/j.jweia.2022.105285.

[49] T. Theodorsen, ‘General Theory of Aerodynamic Instability and the Mechanism of Flutter’, NACA-TR-496, Jan. 1949. Accessed: Apr. 17, 2023. [Online]. Available: https://ntrs.nasa.gov/citations/19930090935